Alma Mater Studiorum  Università di Bologna

DOTTORATO DI RICERCA IN

Scienze Biomediche e Neuromotorie

Ciclo 35

**Settore Concorsuale: 06/I1**

**Settore Scientifico Disciplinare: MED/37**

TITOLO TESI

# MR in vivo tractography for the reconstruction of cranial nerves course

**Presentata da:**

**Laura Ludovica Gramegna**

**Coordinatore Dottorato**

**Prof.ssa  Matilde Follo**

**Supervisore**

**Prof.ssa Caterina Tonon**

**Co-Supervisore**

**Prof. David Neil Manners**

**Esame finale anno 2022**

**Structure of the thesis**

The project presented in my Ph.D. thesis aimed to develop a diffusion tensor imaging tractography algorithm able to visualize the entire course of cranial nerves I ( olfactory nerve) and II (optic nerve and whole anterior optic pathway) allowing both their three-dimensional visualization and their microstructural characterization.
Conventional Magnetic Resonance Imaging of cranial nerves is challenging, and cranial nerveCN trajectory can be intuited only by high-resolution structural sequences and under normal conditions. These nerves are poorly trackable in skull base regions such as ethmoidal cells or in close relationship with a sellar/parasellar tumor.

To overcome this, we first implemented a multi-shell (b values = 0, 1000, 2000) diffusion tensor imaging sequence using a clinical high field 3-T MRI scanner available at the IRCCS Istituto di Scienze Neurologiche di Bologna, Bologna, Italy. We computed a probabilistic reconstruction algorithm (using both in-house-developed scripts and freely available software packages) to create a pipeline capable of reconstructing all nerves of interest, using predetermined regions of interest drawn on the Montreal Neurological Institute (MNI) atlas, and semi-automatically registering the tract on the single structural images.

The newly developed algorithm has been successfully applied in three groups of patients. Firstly, it has been used in patients with persistent hypo/anosmia after COVID-19 infection and healthy controls and showed high rates of CN I visualization. Second, it has been applied to group of patients with sellar/parasellar tumors operated through a mini-invasive endoscopic endonasal approach in which the pre-surgical reconstruction of cranial nerve II and the entire anterior optic pathway has allowed for the improvement of surgical planning. In this study, moreover, the accuracy of the reconstruction was supported by direct visual intra-operative confirmation. Third, the diffusion tensor imaging tractography of cranial nerve II has been applied to a group of patients with genetic optic nerve atrophy (Leber's hereditary optic neuropathy), before and after an innovative genetic therapy, in order to look for changes in DTI properties along the tract.

In this thesis, I will begin by describing the anatomy of the I and II cranial nerves Then, I will describe the basis of the DTI acquisition and of the previous studies in which the tractography of the cranial nerves was applied. I will next describe the work done in the three populations of patients. Lastly, I will make my final conclusions.

# The Cranial Nerves Anatomy

## The Cranial Nerve I

*Anatomy*

Cranial nerve (CN) I (i.e., the olfactory nerve) is composed of solely afferent sensory nerve fibers, is paired and short (ca 28–30 mm in length and 0.5mm in diameter) (López-Elizalde, Campero et al. 2018), and does not project to the brainstem. It originates from the bipolar olfactory neurons in the posterosuperior olfactory epithelium of each nasal cavity. Interestingly, the bipolar olfactory neurons continuously regenerate from stem cells within the basal portion of the epithelium and have a half-life of 30 to 40 days, and the olfactory epithelium has a surface area of 2.5 $cm^2$.

The bipolar olfactory nerve passes through the bony cribriform plate and synapses with the olfactory bulb (OB) and olfactory tracts, which are not myelinated and diverge to form two main bundles, the lateral olfactory stria (responsible for autonomic responses associated with olfaction, such as an increase in salivation and gastric peristalsis/secretion) and the medial olfactory stria (responsible for the majority of functional olfactory transmission through the limen insulae). There, it bends medially to enter the temporal lobe near the uncus, in which lies the primary olfactory cortex (Helwany and Bordoni 2022).

The olfactory nerve itself is formed by the OB and the olfactory tract and runs intracranially within the olfactory groove of the ethmoid bone. The olfactory sulcus, which is located on the ventral surface of the frontal lobe (Maingard and Sharma 2022) and runs in an anteroposterior direction between the gyrus rectus and the orbital gyri, is considered an indirect measure of the olfactory nerve.

Regarding the blood supply, the olfactory mucosa is supplied by both the sphenopalatine artery arising from the maxillary artery and the external carotid artery, as well as the anterior and posterior ethmoidal arteries originating from the ophthalmic artery, a branch of the internal carotid artery. Intracranially, the olfactory nerve receives its blood supply from a branch of the anterior cerebral artery called the olfactory artery (Helwany and Bordoni 2022).

An interesting concept is that olfaction, like taste, is an uncrossed sense, and the projections are predominantly in the same hemisphere, although some axons of the medial stria do cross the midline through the anterior commissure to reach the contralateral side (Martin 2021). Intriguingly, women have higher olfactory capabilities but statistically smaller OB volumes, representing an interesting paradox regarding the link between OB volume and olfactory function (Buschhüter, Smitka et al. 2008).

Regarding the imaging of CN I, the olfactory neuroepithelium present in the in the upper part of the nasal cavities is not discernable using MRI due to its small dimensions, but rarely the olfactory filia linking the extracranial olfactory neuroepithelium to the OB through the openings of the ethmoid cribriform plates can be identified on ultra-high-resolution T2-weighted images or reconstructed constructive interference in steady state (CISS) MRI sequences (Duprez and Rombaux 2010).

**The Cranial Nerve II**

The second CN (i.e. optic nerve) is part of the visual pathway, a group of anatomical structures that allows for vision by transmitting the light stimuli from the photoreceptors of the retina to the primary visual cortex (V1 cortex) in the occipital lobe of the brain. The optic nerve originates from the nuclear cells present in the retinal ganglion whose axons project via the optic nerve, optic chiasm, and optic tract to the lateral geniculate nucleus (LGN). In the LGN there are secondary neurons that project via the optic radiation to the primary visual cortex (Drake, Vogl et al. 2020). For this reason, the visual pathway can be divided into two portions: the anterior visual pathway, which is also called the retinogeniculate pathway (RGVP) (He, Zhang et al. 2021) and comprises the structures from the retina to the LGN, and the posterior visual pathway which comprises the structures posterior to the LGN.

The optic nerve is myelinated by oligodendrocytes, contains only sensitive fibers, and is considered an extension of the central nervous system (Hansen, Netter et al. 2019). After originating in the retina, it emerges from the posterior pole of the eyeball, passes through the optic canal in the sphenoid, and converges with the contralateral optic nerve at the level of the anterior and ventral margins of the optic chiasm, where it terminates.

The fields of view of both eyes, which is defined as the extent of the observable world that is seen at any given moment, are conventionally divided into four quadrants: upper temporal (i.e., lateral), upper nasal (i.e., medial), lower nasal, and lower temporal.

*The retina*

The retina is a thin layer of nervous tissue within the posterior part of the orbit which has the purpose of receiving the light and converting it into neural signals responsible for the mechanism of vision. It includes the retinal ganglion cell (RGC) layer where the somata of the nerves comprising the optic nerve are found.

Anatomically, the retina can be divided into two parts, the nasal medial and temporal lateral, with the macula and fovea at its center which contain the highest RGC density in all primates (Brooks, Komàromy et al. 1999).

The left side of the field of view (the extent of the observable world that is seen at any given moment) projects on the right side of the retina, and vice versa. Objects in the upper half of the field of view form an image on the lower half of the retina, while objects in the lower half of the field of view project upward due to the optic properties of the lens.

Axons arising from RGC run within the retina itself and converge to form the optic nerve at the level of the optic disc. The RGC arising near the fovea and macula centralis are situated more

centrally in the optic disc and nerve, while axons arising from RGC in the peripheral retina lie in the periphery of the optic disc and nerve (Minckler 1980).

***Optic nerve***

The optic nerve itself, which a is defined a white matter tract of the diencephalon composed principally of the axons of RGCs, is about 50 mm long and can be anatomically divided into four segments (Gala 2015):

1. Intraocular (approx. 1 mm): the portion contained within the RGC layer of the retina where nerve fibers are not myelinated (J. Salazar, I. Ramírez et al. 2019).
2. Intraorbital (approx. 25 mm): extends from the posterior pole of the ocular globe to the optic canal in the sphenoid at the apex of the orbit. This segment is surrounded by the three meningeal sheets (dura mater, arachnoid, and pia mater) and its subarachnoid space is in communication with the suprasellar cistern (Gala 2015).
3. Intracanalicular (approx. 9 mm): the portion projecting through the optic canal, accompanied by the ophthalmic artery and the sympathetic nerves.
4. Prechiasmatic (approx. 16 mm): this part of the nerve exits the optic canal and extends backwards and slightly upwards within the subarachnoid space of suprasellar cistern.

Figure 1. Optic nerve division into 4 segments according to Gala et al. 2015.

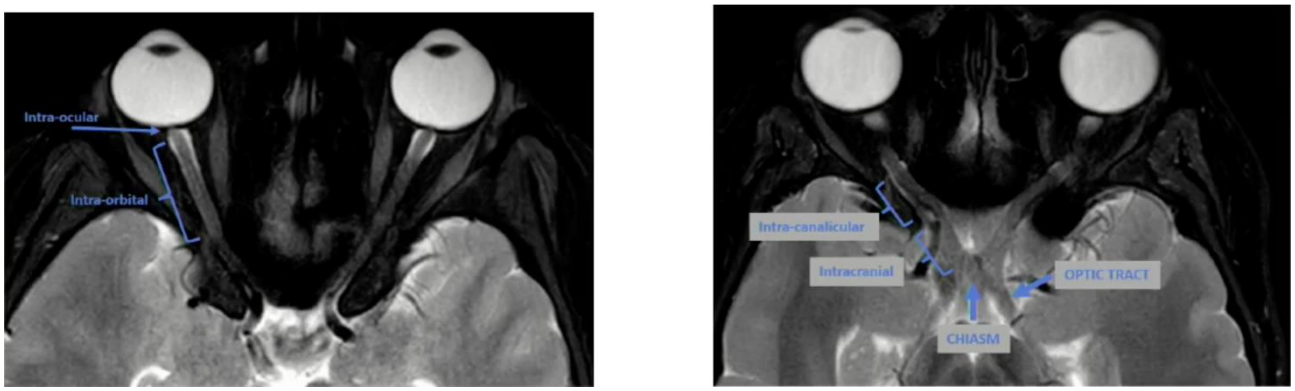


***Optic Chiasm***

The optic chiasm is the anatomical structure where the fibers originating from the optic nerves cross. The fibers composing the medial parts of the optic nerves (called the nasal fibers) cross the midline, while the lateral ones (temporal fibers) remain homolateral. Anatomically, the optic chiasm is situated at the junction of the anterior wall and the floor of the third ventricle, approximately 5–10 mm above the hypophysis.

***Optic Tract***

The optic tracts contain the homolateral fibers of the same optic nerve and the contralateral crossing nerve fibers and originate from the posterolateral part of the optic chiasm. Anatomically,

it curves around the cerebral peduncles of the rostral midbrain and divides into two roots (J. Salazar, I. Ramírez et al. 2019). The first, the lateral root, is larger and terminates posteriorly in the LGN and is responsible for the mechanism of vision. The second is a smaller medial root, which is connected both to the pretectal area and to the superior colliculus in the midbrain and is involved in the visual reflex pathway. Thus, the left optic tract contains fibers from the temporal half of the left retina and nasal half of the right retina, and vice versa.

***Lateral Geniculate Nucleus***

The LGN is an ovoid gray matter (GM) structure located in the postero-inferior part of the thalamus that consists of six laminae or cell layers oriented in a roughly dome-shaped mound. Specifically, nerve fibers derived from the contralateral eye (crossed fibers from the nasal half of the retina) terminate on cell bodies in layers 1, 4 and 6. Those of the ipsilateral eye (from the temporal half of the retina) terminate in layers 2, 3 and 5. Thus, each LGN receives information from both retinae. While each RGC axon may terminate in up to six geniculate cells, these are all located in one lamina. Fibers from the upper quadrants of peripheral retinae synapse on the medial aspect of the LGN and those of the lower quadrant on the lateral aspect. The macula projects to a disproportionately large central wedge of the LGN. Optic radiations originate from the LGN and form the caudal part of the thalamus. Then, they run through the retrolenticular segment of the internal capsule and project dorso-medially to the calcarine cortex (primary visual cortex – V1) where they terminate. The upper optic radiations extend into the parietal lobe, while the lower radiations enter the temporal lobe. Parietal optic radiations carry information from the lower quadrants, while temporal radiations do the same for the upper quadrants.

The primary visual cortex is situated in the occipital lobe (Brodmann area 17) (Naidich, Castillo et al. 2012) around the calcarine scissure (thus it is also called the calcarine cortex). It is the first area of the brain that processes visual stimuli and is responsible for the creation of conscious images. As with the optic radiations, the upper cortex is responsible for the lower quadrants and the lower cortex for the upper ones.

*Functional Organization of the Anterior Visual Pathway*

The fibers from the somata of cells present in each retinal region follow specific courses inside the optic pathway. In particular, the fibers originating from the superior-temporal quadrant of the retina do not cross but project through the ipsilateral CN and tract to the medial part of the geniculate ganglion. The second order neurons starting from the geniculate ganglion course within the posterior bundle of the optic tract and terminate in the central portion of the calcarine fissure (purple and red fibers in A, for the right and left side). Specifically, the fibers beginning in the inferior-temporal quadrant of the retina do not cross but project through the ipsilateral cranial nerve and tract to the lateral portion of the geniculate ganglion. The second order neurons originating from the geniculate ganglion extend within the anterior bundle of the optic tract and terminate in the central part of the calcarine fissure (yellow fibers in A, for the right and left side).

The fibers originating in the superior-medial quadrant of the retina cross the midline in the chiasma and terminate in the medial portion of the geniculate ganglion. The second order neurons run in the posterior bundle of the optic tracts and terminate in the proximal portion of the calcarine fissure. The fibers starting from the inferior-medial quadrant of the retina cross the midline in the chiasma and terminate in the lateral part of the geniculate ganglion. The second order neurons course in the anterior bundle of the optic tracts and terminate in the proximal portion of the calcarine fissure.

The fibers originating from the macula and the fovea extend, along with the corresponding part of the fibers, in the medial portion of the corresponding part of the optic nerves. In the optic radiation, they project in the central bundle and terminate in the most superficial portion of the calcarine fissure (Wärntges and Michelson 2014).

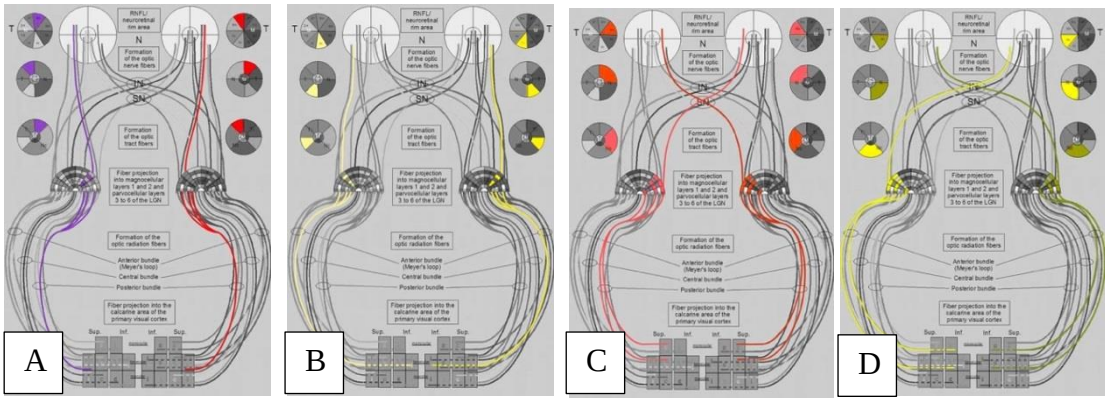


**Figure 2.** In this figure, modified from Wärntges, S. and G. Michelson (2014). "Detailed illustration of the visual field representation along the visual pathway to the primary visual cortex: a graphical summary." Ophthalmic Res 51(1): 37-41, each fiber population originating from a specific retinal region is depicted in a specific color to follow its trajectory. In particular, those originating from the superior-temporal quadrant of the retina are represented in A and those from the inferior-temporal quadrant of the retina in B. On the contrary, those originating from the superior-medial quadrant of the retina are represented in C and those originating from the inferior-medial quadrant of the retina in D.

# Diffusion Tensor Imaging (DTI) and Tractography technique

## Diffusion weighted imaging

The diffusion weighted imaging (DWI) method was originally proposed by Peter Basser (Basser, Mattiello et al. 1994), and the application of the technique in the human brain soon enabled the study and quantitative analysis of the complex anatomy of the white matter fiber tracts (Pierpaoli, Jezzard et al. 1996), becoming the only method for the *in vivo* and non-invasive quantification of water diffusion in biological tissues (Le Bihan and Johansen-Berg 2012).

### ***The concept of diffusion weighted imaging***

Diffusion contrast is based on the concept that signal from a voxel will decrease exponentially as a function of time at a rate depending on the strength of the magnetic field gradients applied between an excitation pulse and signal reception, the duration of the gradients, and the diffusion coefficient of water molecules in the voxel. The first two factors do not vary from voxel to voxel. Within a given acquisition, only intravoxel diffusion (D) varies between voxels, and thus contrast in a diffusion weighted (DW) image is a function of the apparent diffusion coefficient. DWI is only sensitive for motion of water molecules that are aligned with the motion-probing magnetic field gradient applied between excitation and signal reception (Nucifora, Verma et al. 2007).

### ***Isotropic and anisotropic signal in the brain***

DWI is sensitive to the random microscopic motion of water molecules (i.e., diffusion). Water diffusion in the brain is two to 10 times slower than free water diffusion because the tissue microstructure impedes molecular movement (Clark and Le Bihan 2000). In the brain, diffusion is highly influenced by the presence of white matter (WM), which includes bundles of neuronal axons packed in myelin, and this tight “packaging” introduces a directional dependence to molecular motion along the major axis of the bundle (Basser, Mattiello et al. 1994).

By measuring the DWI signal along a number of directions in three dimensions, the degree of directionality, as well as the orientations of these WM fibers, can be inferred (Jeurissen, Tournier et al. 2014). In a liquid where there are no barriers to free diffusion of water, movement is the same in all directions and this free movement of water is termed isotropic diffusion. However, in the presence of highly oriented barriers such as WM fibers in the brain, the diffusion follows a preferential direction, and this is termed anisotropic diffusion (Beaulieu 2002).

## Signal acquisition

### ***Acquisition: Single-shell***

Classical DWI studies have used acquisitions based on magnetic field gradients of varying direction but only one effective field strength ("single-shell" or "single-b value" acquisition). The degree of sensitivity of DWI images to water diffusion is controlled by a user-selectable parameter known as the b-value, which is expressed in unit of s/mm$^2$. The term "b-value" was firstly used by Stejskal and Tanner to describe their pulse sequence consisting of two strong gradient pulses of magnitude (G) and duration (δ), separated by time interval (Δ), used to perform DWI. This pulse sequence still forms the basis for most modern DWI sequences in which a larger b-value is achieved by increasing the gradient amplitude and duration and by widening the interval between gradient pulses (Stejskal and Tanner 1965).

Standard b-values used in conventional DWI are in the range of 700 to 1000 s/mm$^2$ (Baumann, Cammoun et al. 2012) whereas b-values over 1500 s/mm$^2$ are defined as "higher b-values". With the application of larger diffusion gradients (increasing b-value), the DWI signal is reduced relative to thermal noise, i.e., signal-to-noise ratio (SNR) is reduced (García Santos, Ordóñez et al. 2008). However, high b-value DWI provides better contrast owing to its sensitivity to tissue diffusivity and its reduced dependence on T2 sensitivity, a dependence known as the T2 shine-through effect (Seo, Chang et al. 2008).

***Acquisition: Multi-shell***

More recently, a new generation of acquisition paradigms have been developed employing multiple b-values ("multi-shell") (O'Donnell and Westin 2011). By leveraging more than one diffusion-weighting gradient strength, the differential tissue responses elicited by each different b-value can be used to model more detailed features of the different cellular environment in each voxel (Basser, Mattiello et al. 1994, Assaf and Basser 2005).

The differential tissue responses elicited by different b-values allows us to:

- reduce the partial volume effects due to the isotropic contribution from the cerebrospinal fluid (CSF) in some voxels (Castellaro, Moretto et al. 2020)
- reduce the partial volume effects due to the presence of other tissue in the voxels (Pines, Cieslak et al. 2020)
- reduce the partial volume effects due to movement artifacts (Pines, Cieslak et al. 2020).

Moreover, it has been demonstrated that b-values higher than 1000 s/mm$^2$ increase the resolution of WM fibers with high angular curvature because of their anatomy (Tournier, Calamante et al. 2013).

## Signal modelling

### *Signal modelling: Diffusion tensor model*

During DWI of MRI, magnetic field gradients are employed to create an image that is sensitized to diffusion in a particular direction. By repeating this process of diffusion weighting in multiple directions, a three-dimensional diffusion model (called the diffusion tensor) can be estimated (O'Donnell and Westin 2011). The three-dimensional DWI data is fit to a model to create maps of model parameters that allow characteristics of the brain to be visualized. Diffusion tensor imaging (DTI) is the most widely used diffusion "model" for fitting DWI signals and assessing WM orientation and organization (Basser, Mattiello et al. 1994). The DTI model assumes the presence of only one type of tissue (i.e., WM) within each voxel. Therefore, it is invalid in voxels outside the brain itself that contain multiple tissues in the same voxel, as well as in voxels within the brain itself that contain crossing fibers of different WM tracts. It can be applied to voxels in which only isotropic diffusion is present, within the ventricles for example, but it may give inaccurate results.

### *Signal modelling: Constrained spherical deconvolution*

Spherical deconvolution (SD) is one of the models proposed to solve the issue caused by the presence of multiple fiber orientations within the same voxel in DW images. It models the DW data as the sum of a set of spherical harmonic functions (Dhollander *T* 2021).

Constrained spherical deconvolution (CSD) is a method that enables modelling of WM in the presence of multiple fiber orientations (Tournier, Calamante et al. 2004, Tournier, Calamante et al. 2007), even when there are crossing fiber populations within a voxel, and thus offers a means to model complex WM structures more effectively than the DTI model. However, the ability of CSD to model WM may be confounded in voxels also containing other tissues, such as GM or CSF, the so-called partial volume effect (Mito, Dhollander et al. 2020).

The SD model is able to estimate the full fiber orientation distribution function (fODF) in each brain voxel. In other words, it relies on the principle that the DW signal originating from the various fiber populations present in a voxel is given by the spherical convolution of this response function. Moreover, a constraint is commonly introduced in this model to minimize the appearance of physically meaningless negative values in the reconstructed fODF. With this constraint, distinguishing CSD from the simpler SD method, it becomes possible to reduce the noise sensitivity of the model, allowing reliable fODF estimates to be made on clinically feasible DW-MRI data (Dhollander *T* 2021).

However, conventional CSD can provide high quality fODF estimates only in voxels containing exclusively WM, whereas in voxels containing other tissue types such as GM and CSF this model

may produce noisy fODF estimates, the same problem that occurs in DTI. To overcome this challenge, a multi-tissue CSD model has been proposed assuming that four tissues are present in the brain: WM, deep GM (basal ganglia), cortical GM, and CSF. In the case of multi-shell acquisition, signal from each of these different tissues has a unique b-value dependency and this allows better modelling of the fODF in each tissue type.

Diffusion tensor tractography

White matter tractography (WMT) uses information models of DWI data to obtain a 3D representation of fiber architecture in the WM. All tractography methods start from the assumption that, in the human brain, the connections among brain cortical regions are made by myelinated axon bundles, collectively called WM. Tractography algorithms incorporate parameters from the DTI tensor or from the probability density fraction (PDF) by linking neighboring voxels having similar maximum diffusion direction, creating pseudo-axonal tracts that can be used to visualize microstructural orientation (i.e., fiber tracking) (Alexander, A. L. 2010).

There are two main approaches to fiber tracking, called “deterministic” and “probabilistic”. The deterministic method is a computational method that uses the orientation information within the diffusion tensor model, in particular the direction with the greatest diffusivity, called the major eigenvector, to reconstruct the estimates of WM pathways. It assumes that the greatest diffusion in the brain is roughly parallel to the local WM fiber bundle direction. Deterministic tractography tends to be simple and fast, and the most frequently used algorithm, FACT, can be run on a 3D brain image in a few minutes (Mori, Crain et al. 1999). On the other hand, probabilistic fiber tracking methods use more complex, linear propagation approaches, estimating the principal eigenvector direction (Mori and van Zijl 2002) according to a probability distribution function (Lazar and Alexander 2003, Parker, Haroon et al. 2003, Jones and Pierpaoli 2005). The accuracy and precision of both deterministic and probabilistic tractography algorithms are limited by image noise, artifacts, and the presence of crossing fibers (Alexander, A. L. 2010).

***Deterministic tractography***

The general principle of deterministic tractography algorithms is to use the directional information described by the eigenvector of the diffusion tensor model in each voxel as a surrogate of the principal direction of the water diffusion and the underlying WM orientation. A deterministic tractogram is generated by starting from one (or more) "seed" locations, typically within GM, and propagating the trajectories according to the tractography algorithm until the tracts terminate (Alexander 2010).

Criteria must be defined to terminate tracts when they either leave the tissue region of interest or become unreliable (i.e., when the estimates of the major eigenvector begin to have a large variance). Common stopping criteria include the tract entering a region with low fractional anisotropy (FA) (e.g., FA < 0.2) or the trajectory bending more than a prescribed angle in a single step. The FA threshold is typically used to limit the results to regions where the major eigenvector is well defined. The obvious limitation is that FA can be quite low even in regions of WM, including regions of the centrum semiovale where fiber tracts are crossing (Alexander 2010).

Another strategy is to segment the WM from the DTI data or from a co-registered structural (i.e., T1-weighted) image. Regional constraints can be imposed using specific regions of interest along the expected WM tracts (Alexander 2010).

The simplest approach for WMT is based on streamline algorithms originating from the vector field of each major eigenvector. Commonly used algorithms to do so include linear step-wise algorithms, such as FACT (Mori S, 1999). Even if WMT results are often visually stunning, there are many potential sources of errors that can confound the results. Very small perturbations in the image data (i.e., noise, distortion, ghosting, etc.) may lead to significant errors. Those errors include:

- Tract dispersion, which corresponds to the variance of the estimated trajectories that occur in the peripheral parts of the tracts, as the dispersion will increase with the distance from the seed location. The dispersion in tract estimates from image noise is roughly proportional to the distance and inversely proportional to the squares of the eigenvalue differences and SNR (Anderson 2001).
- Systematic error: while the tract dispersion describes the variance or uncertainty in tractography results, systematic errors in tract position estimation are described by the tract deviation and are particularly dangerous for highly curved trajectories. The possibility of a tract deviation is influenced by the step size. In general, the step size should be significantly smaller (an order of magnitude) than the local radius of curvature. For most tractography studies, a step size on the order of 0.5 mm or smaller is likely adequate.
- Crossing fibers: one of the major limitations of WMT based on DTI is the inaccuracy of the single-tensor model in regions of crossing fibers. Crossing WM tracts will cause the estimated

major eigenvectors to cease coinciding with the fiber orientations. Within a voxel containing multiple fibers, the less dominant fiber direction will never be followed.

**Probabilistic tractography**

The principal concept behind probabilistic tractography is the assessment of "connection confidence" of an observed connection. This provides a measure of the reliability of the observations or, in other words, the amount of evidence in the dataset that supports the possibility of a tract existing through the data set (Parker 2010). This increases the detection of branching and dispersion, but we need to account for the reduction of connection confidence with distance.

Probabilistic tractography offers an estimate of fiber orientation function for a given voxel, while taking into account additional information involving the local environment or the entire tract trajectory to assess the likelihood of connection. However, it is important to remember that, in any given voxel, axonal bodies have a natural spread of orientation, which implies the presence of two or more well-defined populations of axonal bodies. We commonly attempt to estimate the dominant orientation of the underlying microstructure and to determine the PDF of fiber orientation from this single best-estimate, using the assumption that higher anisotropy implies higher precision of the fiber orientation estimate (Koch, Norris et al. 2002).

To create an accurate PDF, we should take into account the effects of noise, diffusion sensitization, and other influential factors. There are several methods designed to estimate the uncertainty in fiber orientation from the noise. The "bootstrap method" is one such approach. Bootstrap methods rely on the idea that the "permutation of data samples" associated with a multi-sample measurement approximates the true distribution of the real axons in the voxel. This is achieved with no prior knowledge or assumptions about the statistical properties of the parameters evaluated.

Since the requirement for multi-sample data is impractical for routine use, "model-based" bootstrap methods have been developed that provide close approximations to the data-based bootstrapping methods (Jones 2008). Moreover, it is important to underline that the probabilistic tractography output depends on which of the following models is used and may include a single-fiber model (e.g., the tensor model) or one of the more complex and more reliable models supporting a more complex representation (e.g., the multi-shell models).

Once PDFs are created in each voxel, orientation density fractions (ODFs) are generated to describe the orientational component of the PDF of particle displacement due to diffusion within a voxel, which is in turn influenced by the dimensions of axons (and other microstructures) in the voxel.

It is important to appreciate the concept that the information content of the ODF strongly depends on the data acquisition and, in particular:

- the number of directions of the diffusion sensitization gradients, which influences the orientation resolution available and the number of fiber populations that may be recovered;
- the data noise level (SNR), which affects the sharpness of the PDF (and therefore the precision of tracking and the number of fiber populations that may be recovered);
- the degree of diffusion sensitization (b-value), which affects the ease with which multiple fiber populations may be resolved, and the voxel size, which affects the degree of bulk fiber-bundle partial voluming and the influence of tract curvature on PDFs;
- tracking distance, as the confidence assigned to connections diminishes with distance from the start point. This is not unexpected, as probabilistic methods rely on the information produced by the diffusion imaging experiment within each voxel that contributes to the pattern of connections. For this reason, is very difficult to set a threshold in the map of connection probabilities.

The interpretation of the output of the probabilistic tractography should be done very carefully. In every voxel it is possible to estimate the probability that a connection through the diffusion data exists on the basis of a model of the diffusion signal within the voxels and our model of connection between voxels. For this reason, caution must be used when making definitive statements about the existence (or nonexistence) of an anatomical connection based on the output of any tractography experiment. While probabilistic methods allow us to quantify the weight of evidence that a particular route of connection through the data exists, deterministic methods are unable to obtain this result.

A significant problem in the interpretation of tractography output is the known occurrence of false-positive and false-negative connections. False-negative findings have two main causes. First, the physical size of the tract may be below the resolution of the data acquisition. Second, the tract evaluated may suffer from partial volume effects that are not adequately modeled (i.e., the model of diffusion and/or tractography may be unreliable in case of crossing or kissing fibers). False positives tend to occur from the inadequacies of the modeling process or from artifacts in the data; false positives may be reduced by the use of prior knowledge in the form of constrained probabilistic tractography using two or more “waypoint” regions. A waypoint is an area through which a tract must pass by definition, based on anatomical considerations (Behrens, Berg et al. 2007).

**Diffusion Tensor-derived Results and Metrics Interpretation**

Once DTI data are acquired and the signal is modelled, the system presents two outputs: the three-dimensional reconstruction of the tracts and the DTI metrics inside the tract. Regarding the three-dimensional reconstruction, the results of probabilistic tractography have been beautifully

described by Jones et al. (Jones, Knösche et al. 2013) as follows: "*How confident I can be that if I was to open up the brain and look directly at the white matter, where the map intensity is high, I am more likely to find an actually white matter pathway that travels back to the point X, compared to the case when the intensity is low.*"

Regarding the DTI-derived metrics, the FA is considered to reflect the signal change when a motion-sensitizing gradient is applied along a given axis, and is influenced by the myelination, the axon density, the axon diameter, the permeability of the membrane — but also, and importantly, the way in which the axons are laid out within the voxel (Jones, Knösche et al. 2013). Regarding the mean diffusivity (MD), is has been proposed the length of the axonal membrane is the strongest independent predictor of the hindered diffusivity within the biological tissues (Eida, Van Cauteren et al. 2016). These concepts will be further discussed below.

***Three-dimensional reconstruction***

As previously described, DTI is capable of measuring the dephasing of spins of protons according to the presence of structures that spatially vary the magnetic field (gradients). The application of tractography in the brain starts from the assumption that, in the human brain, the main barriers responsible for the this change in the directionality of diffusion are the myelinated WM tracts.

Therefore, the first assumption used by tractography is that the peak in the ODF estimated from the data modelled by the CSD runs parallel to the WM fiber tract. However, if we consider the fact that the ODFs are sampled in a grid of voxels, and in each voxel, there is more than one ODF, the reconstruction of continuous trajectories requires the interpolation of the data from each of the continuous voxels; in order to do this, some parameters must be previously established such as the maximum angle that the trajectory might turn. In order to reasonably assume that our signal (the peak in ODF) is maximally tangential to, and can therefore truly reflect, the anatomical fiber orientation of the WM tracts, we must be sure the b-value is sufficiently high to be sensitive to the sharp angularly orientated fibers without lowering the SNR below the value of 3. Additionally, we should utilize at least 30-40 diffusion gradient directions, and we should establish a spatial resolution for the voxels that is as small as possible to reduce the possibility of the presence of different tissues within it.

It is important to emphasize that, in any given voxel, the signal does not inform about the relative positions of different fiber populations within that voxel. For example, it is impossible to distinguish between "kissing" and "crossing" fibers: the DW signals from two bundles of fibers arranged in a given voxel with a letter 'T' configuration, a letter 'L' configuration, or a '+' sign configuration will be identical. It is also crucial to be mindful of the possibility that different tissues may be present within a given voxel and, in particular, of the impact of CSF contamination. Given that CSF is isotropic and has a MD that is approximately as large as free water in tissue, it is clear that any extent of partial volume contamination of the voxel by CSF will bias findings.

The two most important ways to mathematically represent the dependence of the DWI on the biological membrane are the diffusion ODF (dODF) and the fiber ODF (fODF). Considering the dODF, this parameter measures the probability density that a particle will move in a certain direction. Regarding fODF, this parameter describes the diffusion within each voxel, estimating the relative fiber density over the orientation space in an attempt to infer the angular distribution of fiber orientation from the angular structure of the signal.

The "diffusion tensor model," the classic unimodal anisotropic gaussian model, gives a satisfactory approximation when the voxel contains a single co-axial fiber population. However, in any given voxel it is more likely that multiple fiber types will be present, in which case more complex modeling should be utilized.

The final three-dimensional tractography reconstruction we see reflects the attempt of the methods to combine the signal in each voxel (either derived from the principal eigenvector of the diffusion tensor, the peaks in the dODF, or the peaks in the fODF) in order to compute trajectories or pathways through the data, assuming that they run parallelly to the WM bundle below.

***Mean diffusivity (MD) definition***

As previously discussed, the phenomenon of diffusion describes the random movement of molecules in a solvent. Whereas in a hypothetical boundary-free medium the diffusion of molecules depends only on the molecule size, the temperature, and the medium viscosity, in biological tissues water diffusion is hindered by extracellular and intracellular components, classically considered to be fibers and membranes (Einstein 1905, Le Bihan 2013).

Traditionally, it has been thought mechanistically that the reduction of water diffusivity in biological tissue resulted from the collision of water molecules into the cellular membrane barrier. Subsequently, it has been demonstrated that membranes "reduce" the water diffusivity according to their permeability (Le Bihan 2007). However, the exact critical determinant of water diffusion hindering in biological tissue have not been unequivocally identified. A recent *in vitro* study (Eida, Van Cauteren et al. 2016) in various cell lines compared the diffusivity properties of cells dying through apoptosis and necrosis. In apoptotic cells, the cells death is associated with a progressive reduction of cellular volume, chromatin condensation, and nuclear fragmentation, but the plasma membrane remains intact until a very late stage in the process. In necrotic cells, the cell undergoes organelle swelling, plasma membrane rupture, and increased cellular volume. The results of this study give interesting insight on this topic. It demonstrated that, in different cell lines, the relationship between the apparent diffusion coefficient (ADC), the corresponding value for MD, and cellular area depends on the volume of the nucleus (and the nucleus-to-cytoplasm ratio), as the nucleus hinders diffusivity (Tadakuma, Ishihama et al. 2006, Capoulade, Wachsmuth et al. 2011). It also showed that cells with more plasma membrane have reduced diffusion, and that ADC is reduced near the various membranes (Eida, Van Cauteren et al. 2016).

***Fractional Anisotropy (FA) definition***

The definition of FA (Jones, Knösche et al. 2013) within DTI tractography relies on two important classes of factors. The first is that the random displacement of water molecules depends on biological factors such as fiber diameter (i.e., axon diameter), fiber density (i.e., packing density), membrane permeability, and myelination, all of which are modifiable by various diseases. The second is the intra-voxel orientational coherence of any boundaries which depend on anatomical constraints, i.e., the way in which the axons are laid out within the voxel. Consider two voxels, A and B, in the WM, each of which comprises N fibers. In both voxels, the axon diameter, membrane permeability, and myelination of each axon is the same; therefore, at the ultrastructural level, the 'integrity' of each axon is identical. However, in voxel A, all of the axons are aligned along the same axis and densely packed, while in voxel B the axons are much less coherently organized with a range of orientations (such as might arise from fibers fanning, branching, crossing, and/or twisting). The anisotropy of the tensor fitted to voxel A will be much higher than that of voxel B; however, it would be a complete fallacy to argue that the microstructural integrity was lower in voxel B.

In each experimental condition there will be a certain number of voxels that have more than one fiber population, and this depends on the data acquisition, voxel size, and anatomical structure being analyzed. Our ability to differentiate those different fiber populations depends on the model and analysis pipeline used. For example, the angular resolution applied to the sampling scheme, the b-value, and the SNR will impact the minimum resolvable inter-fiber angle and, therefore, the number of distinct fiber voxels that can identified within a voxel.

## Previous Tractography Studies of Cranial Nerves

There have been a few attempts in the literature to perform a tractography of CN I, primarily using specific targeted acquisition sequences with long acquisition times.

In 2011, Skorpil et al. (Skorpil, Rolheiser et al. 2011) used a target sequence with small field of view (b-value of 900 s/mm$^2$, 32 diffusion encoding, repetition time [TR] = 6698 ms, echo time [TE] = 83 ms, FoV 2.3 cm, scan time sequence time was 13.31 minutes) to depict the olfactory tract in five healthy controls. More recently, Echevarria-Cooper et al. (Echevarria-Cooper, Zhou et al. 2022) utilized a specific readout segmentation of long variable echo-trains (RESOLVE) DTI sequence with small field of view to minimize image distortions in the ophthalmic tract (TR = 6250 ms; TE = 61 ms, field of view [FoV] = 240 mm; matrix size = 240 × 240 × 138 mm; 90 DW directions at b = 1000 s/mm$^2$, scan duration: 1h 30 min. The authors analyzed the signal with a CSD model and reported a successful reconstruction in 25 healthy human participants. Neither of the previous studies commented on the anatomical validation of the reconstructed tracts.

Diffusion tensor tractography (DTT) is particularly challenging to perform in the anterior optic pathway including CN II. In fact, the anterior optic pathway exhibits several anatomic features that increase the risk of creating the so-called partial volume effect. These features include the CN II passing through the optic canal and the supracisternal sella where there is a high risk of contamination within the same voxel of other structures such as CSF, air, and bone. Moreover, there are crossing fibers at the level of the chiasma, and commonly used tractography models are unable to distinguish kissing from crossing fiber configurations. Furthermore, fibers originating from the optic nerve curve sharply within a single voxel at the level of the chiasm, another situation that cannot be accurately represented by the DTT models since the tractography algorithm connects voxels that share a coherence in diffusion orientation. For this reason, most tractography algorithms often stall at fiber crossings or high-curvature regions, either because the estimated anisotropy does not exceed a fixed threshold or because of a built-in bias against high-curvature tracts in the form of the angle threshold. Additionally, instances of convergence (multiple bundles merging into one) and/or divergence (a bundle splitting into two) cannot be distinguished. In voxels where convergence takes place, information is lost about which fibers merge into the main tract and which continue on. Similarly, at sites of divergence it is unclear which axon bundles leave the main tract and which continue along it. To date, all of these issues have hindered the development a robust and automated reconstruction pipeline for anterior optic tractography.

**Previous Cranial Nerve II Tractography Studies in healthy controls**

Interestingly, the first attempt to perform tractography of the anterior optic pathway dates back to 2007 when Roebroeck and colleagues (Roebroeck, Galuske et al. 2008) attempted to analyze three samples of *ex vivo* formalin-fixed human chiasm at 9.4 Tesla MRI using a multi-shot pseudo-

3D double spin-echo echo-planar imaging (SE-EPI) with TR/TE = 2000 ms, TR = 35 ms, six gradient directions, and a very small field of view (2×2×2 cm) centered over the chiasma, that allowed for a resolution of 156 × 156 × 312 μm. At that time, only diffusion tensor models were available for interpretation of the signal. Upon examining the streamlines generated, the authors found that in their experiment the decussating fibers do not cross the chiasm in an exclusively diagonally oriented-path but instead follow highly curved paths. This was particularly true in the most lateral aspect of the central chiasm, where some streamlines originating from the contralateral optic nerve slightly curve anteriorly towards the contralateral optic nerve before reaching the contralateral optic tract. Moreover, as expected, in the central portion of the chiasm it was impossible to distinguish the fibers originating from the right and left optic nerves due to the prevalence of converging streamlines from the two fiber groups.

A few years later, Hofer et al. (Hofer, Karaus et al. 2010) used a relatively new developed DW single-shot stimulated echo acquisition mode (STEAM) MRI sequences which rely on radiofrequency-refocused stimulated echoes in order to reduce the magnetic field inhomogeneities. In this method, they added partial Fourier and parallel imaging strategies to increase the SNR, and achieved a 1.8-μm isotropic resolution. Six healthy controls were scanned but, despite all of these precautions, in most cases false-positive streamlines were observed travelling along the optic nerve and jumping over to a neighboring eye muscle, namely the medial or lateral musculus rectus, the course of which closely parallels that of the optic nerve because the DTI available algorithm was unable to avoid “kissing” effects between the optic nerve and neighboring eye muscles. Nevertheless, this was the first study able to demonstrate the visualization of the entire human visual pathway in its full anterior–posterior extension (anterior and posterior pathways).

In 2010, Akazawa et al. (Akazawa, Yamada et al. 2010) used the optic chiasm as an example of a structure with a high density of crossing fibers to test the hypothesis that changing between four different b-values from 700-1400-2100-2800, while maintaining a constant number of diffusion-sensitive gradients (n = 23 directions) influenced the differentiation of crossing fibers at 1.5 Tesla. For this purpose, they scanned 10 healthy volunteers using single-shot echo-planar imaging (TR = 5000 ms; TE = 55, 65, 72, and 78 ms), 32 gradient directions, b-values of 700, 1400, 2100, and 2800 s/mm$^2$, and a voxel size of 3.0 × 3.0 × 3.0 mm. The evaluation of the quality of the crossing fiber reconstruction was done using a visual scoring system (grading from 0 [none] to 3 [excellent]). The study found no differences between the four b-values evaluated. Since it is now well known that the angular resolution of the algorithm depends on the the b-values themselves rather than from the number of gradients, this negative result may have occurred due to the subjective way of quantifying successful crossing fiber reconstruction. Moreover, since TEs differed for each of the b-values, SNR values would also have varied for each of the models, and this was not taken into account in the analysis. The authors acknowledged this as a limitation of the study.

In 2012 Maleki et al. (Maleki, Becerra et al. 2012) were the first to apply CSD to a standard DTI acquisition model (TR = 7900 ms, TE = 92 ms, matrix size = 1.75 x 1.75 x 2.5 mm, b-value = 1000

s/mm$^2$, 72 gradient diffusion directions). However, the publication reported only that the optic tracts had been successfully reconstructed using the chiasm as a starting region of interest (ROI), as the study was focused on the posterior optic pathway.

Kamali et al. (Kamali, Hasan et al. 2014) were able to reconstruct the chiasma and optic tract in five healthy volunteers (while purposely excluding the optic nerve) in a clinical 3-Tesla scanner using DTI acquisition (TR = 14460 ms, TE = 60 ms, b-value = 500 s/mm$^2$, matrix size = 2.29 x 2.29 x 1 mm interpolated at 1 x 1 x 1 mm, and a freely available deterministic algorithm [FACT]).

Kammen et al. (Kammen, Law et al. 2016) pioneered the use of cutting-edge multi-shell HARDI acquisition data from the Human Connectome Project including DTI acquisition with three b-values (1000, 2000, 3000 s/mm$^2$) from 270 gradient directions and 1.25-mm isotropic voxels. Data were acquired in 215 healthy controls, and fiber orientation distribution (FOD) models were computed using an internally developed algorithm. The FOD is a function of the unit sphere whose value represents the probability of fiber tracts occurring along any given direction. The authors did not explicitly state the number of patients for which the reconstruction was successful, but in all images the pathway was evaluated beginning at the chiasm and the optic tracts and excluding the optic nerve inside the orbits.

Jin et al. (Jin, Bao et al. 2019) compared the performance of two methods of signal modelling, namely standard DTI and generalized q-sampling imaging (GQI); GQI is a method of Q-sample imaging based on the Fourier transform relationship between the diffuse MR signal and the potential diffusion displacement. They included five healthy controls and utilized standard DTI acquisition (TR = 800 ms, TE = 108 ms, b-value = 1000 s/mm$^2$, 25 gradient diffusion directions, voxel size = 1 x 1 x 2.4 mm). The validation of the quality was made through visual examination and the quality of the reconstruction was reported to be better in the chiasm using GQI modeling rather than the standard DTI.

Certainly, the most comprehensive study regarding the performance of DTT of the anterior optic pathway was published by He et al. (He, Zhang et al. 2021) in 2021. The authors included 57 patients from the Human Connectome Project scanned with a multi-shell DTI sequence (TR = 5520 ms, TE = 89.5 ms, voxel size = 1.25 × 1.25 × 1.25 mm isotropic voxels, b-values = 1,000, 2,000, 3,000 s/mm$^2$). However, they used only the data deriving from the b = 1000 shells, in order to remain as close as possible to the parameters acquired in clinical practice. In the absence of a defined method to model the signal of the acquired data, four tractography methods were tested: two in the CSD tractography framework (SD-Stream and iFOD1), and two within the unscented Kalman filter (UKF) tractography framework (UKF-1T and UKF-2T). Moreover, several different methods of possible validation of the results were selected as well. First, they utilized a weighted Dice (wDice) score to measure the spatial overlap between the tractographic reconstruction of each method against manual segmentation; the wDice score extends the standard Dice score to account for the number of fibers per voxel such that it gives higher weighting to voxels with dense fibers. Second, one expert visually judged the overlap of the reconstruction over the 3D

magnetization-prepared rapid acquisition with gradient echo (MPRAGE) T1 reconstruction using the open-source 3D SLICER software. Interestingly, no tractography method exceeded the others in all methods of evaluation tested, but the UKF-2T tractographic method was judged to better correspond to the known anatomy by the expert rater.

**Previous Cranial Nerve II Tractography Studies in patients**

All of these DTI-based tractography methods for reconstruction of complete fiber tracts in three dimensions have captured the attention of clinicians as tools for pre-surgical planning. It was recognized that they had the potential to assist the neurosurgical procedure using neuro-navigational systems. The first potential application was in the field of optic pathway glioma in the pediatric population, in order to determine whether it was possible to distinguish the locations of the preserved visual pathway fibers adjacent to the tumor.

In 2012 Lober et al. (Lober, Guzman et al. 2012) were the first to attempt the retrospective reconstruction of the anterior optic pathway in 10 pediatric patients with optic glioma using a standard MRI acquisition (25 isotropic direction with b-values = 1000 s/mm$^2$ and a 3-mm thickness) and a deterministic software (InVivo Dynasuite). Interestingly, the authors found that two patients had unexpected displacement of the non-tumor fiber bundle by the chiasm, and this might have been helpful for the pre-operative planning if they had been identified before surgery.

In 2015 Ge et al. (Ge, Li et al. 2015) prospectively included 10 patients with pediatric optic chiasmatic glioma who underwent DTI (acquisition parameters: 30 diffusion gradient directions, isotropic 2-mm voxels, b-value not reported) of the anterior optic pathway using a deterministic tractography algorithm. The authors achieved a 90% success rate in the reconstructions. They were able to display different positional relationships to the tumor (i.e., some were predominantly located in the bilateral walls of the tumor, some had a discontinuity or traveled through the tumor). The authors reported a 100% coincidence with the intraoperative findings.

In 2018 Hales et al. (Hales, Smith et al. 2018) published a case series of 21 pediatric patients with anterior optic glioma in which the anterior optic pathway was reconstructed using a CSD method analysis of a multi-shell acquired paradigm (b values =1000 and 2000 s/mm$^2$, 60 gradient diffusion directions). The authors did not comment on the quality assessment of the reconstruction, but reported a significant correlation between the reduction in FA in the optic nerve and visual acuity in the corresponding eye.

One other clinical application of anterior optic pathway tractography is in patients with multiple sclerosis (MS). The anterior optic pathway is an important site of MS disease activity, as optic neuritis is a common onset manifestation, and approximately 50% of patients are estimated to develop an episode of optic neuritis during their lifetime (Dasenbrock, Smith et al. 2011). In addition, subclinical damage throughout the entire optic pathway has been widely documented (Sisto, Trojano et al. 2005).

The study by Techavipoo et al. (Techavipoo, Okai et al. 2009) was the first to successfully reconstruct, with excellent anatomical fidelity, the complete anterior optic pathway in 16 MS patients with variable clinical presentation and visual function deficit as well as in seven healthy volunteers. The computation of diffusion metrics showed significantly reduced FA values and increased radial diffusivity (RD) values, both interpreted as biomarkers of reduced myelin integrity, in nerves and optic tracts in a subgroup of MS patients with optic neuritis and reduced visual function, compared with other subjects, both healthy and affected, in whom visual function was normal. An association was subsequently identified between such changes in metrics and failure to recover visual function following the episode.

The work of Naismith et al. (Naismith, Xu et al. 2012) also demonstrates how diffusion metrics may predict the clinical course of patients with MS and optic neuritis. Indeed, lower axial diffusivity (AD) values in the optic nerve at onset correlated with worse recovery of visual function after six months, as assessed by visual acuity, 5% contrast, and Pelli-Robertson tests. These values are also associated with findings at instrumental exams commonly used in clinical practice to evaluate these patients and are suggestive of greater nerve fiber damage, namely reduced retinal nerve fiber layer thickness on optical coherence tomography (OCT), and lower amplitude and greater latency of visual evoked potentials (VEP). Conversely, RD and FA values are predictive of outcomes for patients who have had a remote episode of optic neuritis: at one-year, higher RD and lower FA values were found in subjects who had incomplete recovery of visual function, compared with those in whom it was complete.

# Cranial Nerve I tractography in post-COVID-19 persistent hyposmia patients

**Introduction**

In December 2019, a global pandemic began worldwide due to the infection caused by the coronavirus SARS-CoV-2 (WHO 2020). In mild cases of COVID-19 infection, the presence of hyposmia or anosmia in the absence of nasal discharge and conductive obstruction of the olfactory cleft (i.e., upper parts of nasal cavities) has been shown to be a hallmark of the disease (Collantes, Espiritu et al. 2021). It has been proposed that SARS-CoV-2 enters the olfactory sensory neurons through the olfactory mucosa and continues its way through the cribriform plate to reach secondary olfactory neurons in the OB (Mehraeen, Behnezhad et al. 2021). However, it was not elucidated whether the mechanism causing olfactory dysfunction (OD) is due to alterations in the cells of cranial nerve in the OB and tract itself or its direct action in brain primary olfactory cortices.

A recent review including ten studies and a total of 183 COVID-19 cases and 308 healthy controls without COVID-19 suggested no difference in the volume of OBs in COVID-19 patients (Mohammadi, Gouravani et al. 2022).

**Aim**

This portion of my thesis project sought to determine the capability of a whole-brain acquisition of DTT to depict microstructural differences within CN I in patients with persistent post COVID-19 OD.

**Methods**

*Study population*

We prospectively recruited consecutive patients referred at IRCSS Istituto delle Scienze Neurologiche di Bologna from February 2021 to November 2021 for persistent (≥ 1 month) OD with onset during COVID-19 infection, confirmed by an antigen or molecular-based test for SARS-CoV-2. Patients with preexisting OD and chronic rhinosinutis were excluded. In a single day, each participant underwent an olfactory and neuropsychological assessment, and a brain MRI examination.

*Olfactory function assessment*

Patients were thoroughly interviewed on symptoms of OD, either quantitative (hyposmia and anosmia) or qualitative (dysosmia, including parosmia, cacosmia, and phantosmia), and associated gustatory dysfunction. Subsequently, olfactory performance was evaluated objectively with the standardized “Sniffin’ Sticks” test (Burghart Messtechnik, Wedel, Germany) (Kobal, Hummel et al. 1996). This consists of three subtests: olfactory threshold (T), odor discrimination (D) and odor identification (I), each with a score ranging from 1 to 16. “TDI” represents the summative score of the three components, ranging from 3 to 48. Olfactory function is categorized as functional

anosmia (TDI score ≤ 16), hyposmia (TDI score between 16.25 and 30.5), or normosmia (TDI score ≥ 30.75, with “supersmellers” scoring ≥ 41.5 points) (Oleszkiewicz, Schriever et al. 2019).

*Neuropsychological assessment*

Years of education and handedness dominance using the Edinburgh Handedness Inventory (EHI) (Oldfield 1971) were calculated for all patients and controls. EHI scores between -1 and 0.5 were considered indices of left-handedness, right-handedness was defined by scores between 0.5 and 1, and scores between - 0.5 and 0.5 indicated ambidextrousness.

All patients were administered a standardized neuropsychological battery including a general screening test (i.e., Montreal Cognitive Assessment MoCA) (Nasreddine, Phillips et al. 2005). Language skills were assessed using an Associative Fluency Test (Carlesimo, Caltagirone et al. 1996) and a Category Words Fluency Test (Novelli, Papagno et al. 1986). Verbal and visuo-spatial short-term memory span were assessed using respectively the Digit Span Forward test (Milner 1971) and the Corsi Block Test (Milner 1971). In addition, verbal memory (short-term and long-term) was investigated using the auditory verbal learning test (AVLT) (Rey 1964), while semantic memory was specifically explored using the naming to verbal description sub-test of the Sartori Semantic battery (Barletta-Rodolfi, Gasparini et al. 2011). Visuo-spatial long-term memory was examined by the delayed recall of the Rey-Osterrieth Complex Figure (ROCF) (Caffarra, Vezzadini et al. 2002). Repeating the ROCF further explored the patients’ visuo-constructional abilities. Attention and executive functions were assessed by administrating the Stroop test (Caffarra, Vezzadini et al. 2002), the Trail Making Test (TMT) A & B (Reitan and Wolfson 2001), and the Digit Span Backward test (Orsini and Laicardi 1998). Furthermore, the Depression, Anxiety and Stress Scale - 21 Items (DASS-21) (Lovibond and Lovibond 1995) was used to measure the emotional states of depression, anxiety, and stress. The Modified Fatigue Impact Scale (MFIS) (Larson 2013) was used to evaluate how fatigue was affecting patients with long COVID-19 symptoms.

**MRI acquisition**

*MRI specifications*

Images were acquired using a 3T MRI Scanner (Magnetom Skyra, Siemens, Erlagen, Germany) and VE11C-SP01 software (maximum gradient amplitude 45 mT/m; maximum "slew rate" 200 T/m/s) and a 64-channel phased head coil at the IRCSS Istituto delle Scienze Neurologiche di Bologna – Ospedale Bellaria, Bologna.

*Subject preparation*

Written informed consent was obtained from each participant before MRI examination. Participant removed all metallic or non-MRI compatible object before being positioned on the scanner bed in a head-first supine position. Participants were instructed to abstain from rotating their heads inside the coil. Head position was further restricted using foam pads. They used phono-absorbent earplugs to protect their ears from the high noise level. They were also given a bell to ring in case of emergency. The receiver coil has a mirror that allows the patient to see the control room and reduce the effect of claustrophobia.

*Scan protocol*

A standardized scan protocol was followed in which at least the following sequences were acquired.

T1-weighted images acquired using a three-dimensional inversion recovery prepared spoiled gradient-echo (3D MPRAGE) sequence (flip angle = 9°; inversion time [TI] = 900 ms; TE = 2.98 ms; TR = 2300 ms; acquired matrix size = 256 × 256 × 256; phase FoV = 100%; reconstructed voxel size = 1 mm isotropic) were used as an anatomical reference. DTI multi-shell acquisition was performed employing a single-shot spin-echo echo-planar imaging (EPI) sequence with two different phase encoding directions (to better average the useful signal and eddy currents), antero-posterior (A-P) and postero-anterior (P-A) (TE = 98 ms; TR = 4300 ms; 87 contiguous 2-mm thick slices; FoV = 220 × 220 mm; acquired matrix = 110 x 110; reconstructed in-plane resolution = 2.0 mm) with diffusion sensitizing gradients applied in 131 (A-P) and 49 (P-A) non-collinear directions, 8 b = 0 s/mm$^2$ (A-P and P-A), 12 b = 300 s/mm$^2$ (A-P and P-A), 30 b = 1000 s/mm2 (A-P and P-A), 64 b = 2000 s/mm$^2$ (A-P) volumes.

**Diffusion tensor tractography analysis**

*Imaging preprocessing*

Data from each participant were preprocessed using an in-house automated pipeline developed from software packages freely available as part of the Oxford Functional Magnetic Resonance Imaging Software Library (FSL), version 6; the NIH Analysis of Functional NeuroImages (AFNI), version 20.3.02; and MRtrix, version 3.0.2.

DW images were skull-stripped using the FSL "bet" tool. Image denoising was performed with the MRtrix3 "dwidenoise" function (Veraart, Novikov et al. 2016), implementing a principal component analysis approach. Susceptibility-related distortions in the EPI acquisition were estimated using the FSL "topup" function; subsequently, a combined correction for susceptibility,

eddy-current effects, and signal dropout, most commonly induced by subject movement, was performed by FSL “eddy_openmp,” based on the “topup” estimates.

The DWI data were modelled at the voxel level using functions of the MRtrix toolkit. In particular, the response function for SD was modelled using the “Dhollander” algorithm within “dwi2response” (Dhollander, Mito et al. 2019). Fiber orientations distributions were estimated using multi-shell multi-tissue SD using the “msmt_csd” method implemented in the “dwi2fod” function (Jeurissen, Tournier et al. 2014), as described in Manners et al., 2022 (Manners, Gramegna et al. 2022).

Characterization of the diffusion properties of tissue within each voxel was provided by FSL “dtifit” based on the diffusion tensor, which was used to estimate voxel FA and MD.

*Tract estimation*

Tractography is a method that converts volumetric maps of diffusion characteristics into estimates of the probable locations of WM tracts based on the generation of streamlines linking adjacent voxels. The MRtrix tool “tckgen” generated these streamlines by a first-order integration over fiber orientation distributions (iFOD1) approach (Tournier, Calamante et al. 2012), following the procedure described by He et al. (He, Zhang et al. 2021).

In order to isolate the olfactory pathway, selected fibers were transformed to the Neuroimaging Informatics Technology Initiative (NIfTI) format to create a volumetric probability map based on fiber density. Voxels were subjected to a threshold that excluded low probability tracts as detailed in the following section.

**Olftactory nerve reconstruction**

*Processing*

On the Montreal Neurological Institute 152 (MNI152) standard brain, a mask including all the trajectory of the whole anterior olfactory pathway from the OB through the olfactory tract to the olfactory stria (called “NERVO_mask.nii.gz”) was drawn. A single automatic exclusion ROI including all the possible spurious segment originating from the principal tract (called “ROI_NERVO_excl.nii.gz”) was then created. Next, a seed in the proximal part of the OB (“ROI_I_start.nii.gz”) and a target in the more distal part of the OB ("ROI_I_end.nii.gz”) and at the level of the olfactory cortices were drawn.

A linear-affine registration was performed between the $b_0$ image of the DTI and the 3D MPRAGE T1 using the “flirt” tool in FSL, and one non-linear (using “fnirt” of FSL) between the 3D MPRAGE T1 and the MNI, in order to achieve an indirect transformation between the $b_0$ image and MNI. This registration is applied to each ROI with the “applywarp” function (using the “nearest neighbour” approach for the mask and the exclusion and the “trilinear approach” for the others). For each hemisphere (Left = L and Right = R), the iFOD1 (“tckgen”) method was applied to generate up to 5,000,000 streamlines from the START ROI (seed), then selecting only those

fulfilling specified criteria: angle ≤ 10°, cutoff/seed_cutoff = 0.005. The seeding eventually stopped if 2000 tracks per hemisphere were selected according to the above constraints. The same procedure was repeated after inverting the seed and the target and the pairs of corresponding tracks by seed and target were added into a single tract. The tracts were then transformed into an image in the NIfTI format, where the voxel intensity was proportional to the density of the streamlines; a threshold set to at least 10% of the maximum value was applied to obtain the "final_nifti".

*Along-tract analysis*

In order to perform the along-tract analysis, the "final_nifti" file is used to mask each of the streamline file defining the two olfactory nerves (right and left). For each nerve, the streamline file is registered to the MNI using the "tcktransform" option. Two points are defined as the most extremal points that are reached by at least 50% of the fibers in the anterior and posterior directions. To identify these points, the nerve is cut in each slice of the NIfTI image in the main direction of the nerve (typically the y-axis) and the number of streamlines passing through each slice is calculated using the "tckedit + tckstats" option of MRtrix (Tournier, Smith et al. 2019). The two identified extremal points of each track define a line, which is used to do the resampling (using the "tckresample" function) of each line in six (n=6) equidistant points.

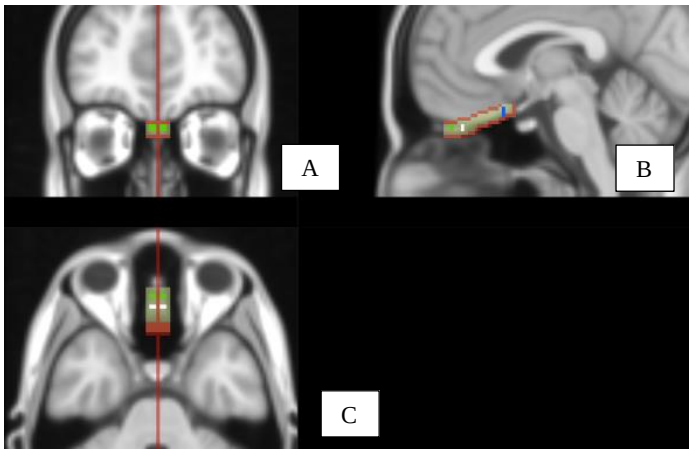


Figure 2: Coronal (A), sagittal (B), and axial (C) reconstruction of the study template for the CN I reconstruction. In yellow: the mask including the trajectory of the entire anterior olfactory pathway from the olfactory bulb, through the olfactory tract to the olfactory stria. In red: the mask is surrounded by a single automatic exclusion region of interest drawn to exclude all the possible spurious segments originating from the principal tract. Within the mask, a seed was placed in the proximal part of the olfactory bulb (in yellow) and a target in the more distal part of the olfactory bulb (in blue).

**DTI metrics evaluation**

For each of these six points the MD and FA were calculated. For each side, the median values of each olfactory nerve were generated.

**Statistical analysis**

Continuous variables are expressed as mean and standard deviation (SD), while categorical variables are expressed by absolute numbers (n) and percentages (%). Groups were compared using Student's t-test or Mann-Whitney U test, as appropriate, for continuous variables and Pearson chi-square test or Fisher's exact test, as appropriate, for categorical variables. DTI metrics were compared between patients with post-COVID-19 persistent hyposmia and controls using an unpaired t-test.

**Results**

*Study population*

A total of 23 patients presenting with persistent COVID-19-related OD were included and underwent olfactory assessment, neuropsychological evaluation, and brain MRI. Mean age was 37 ± 14 years, 12 (52%) were females. Mean duration of OD was 11 ± 5 months, with a maximum of 19 months. In all patients was present an olfactory defect, associated with dysosmia in nine (39%) cases, and with gustatory dysfunction in 19 (83%) cases.

*Neuropsychological evaluation*

Memory and executive functions were the two cognitive domains mainly impaired. Specifically, short-term and long-term verbal memory were impaired in 9% and 13% of patients; while short-term and long-term visuospatial memory were impaired in 9% and 17% of patients. Moreover, regarding the executive function domain to inhibit cognitive interference and working memory, deficits were found respectively in 10% and 13% of patients.

Almost one-third of the patients had a pathological depression score, while three-fourth of patients had a pathological fatigue score. Positive significant correlations were found between odor discrimination and executive function abilities: attentive abilities (i.e., Trail Making Test A; $r = -0.631$, $p = 0.001$) and cognitive flexibility (i.e., Trail Making Test B; $r = -0.768$, $p < 0.001$).

*Neuroradiological evaluation*

The reconstructed CN tractography reconstruction of CN I were superimposed on the 3D MPRAGE T1 images and anatomically validated by expert neuroradiologist as corrected.

*DTI metrics*

MD

Among post-COVID-19 patients with persistent hyposmia the mean olfactory nerve MD value was $1.17 \pm 0.36 \times 10^{-3}$ $mm^2/s$ on the right and $1.13 \pm 0.29 \times 10^{-3}$ $mm^2/s$ on the left. Among healthy controls the mean olfactory nerve MD value was = $1.21 \pm 0.3 \times 10^{-3}$ $mm_2/s$ on the right and = 1.23

± 0.26 x $10^{-3}$ $mm^2$/s on the left. No significant difference was found between patients and healthy controls (p = 0.670 for the right olfactory nerve, p = 0.195 for the left).

FA

Among healthy controls the mean olfactory nerve FA value was 0.223 ± 0.046 on the right and 0.215 ± 0.049 on the left. No significant difference was found between patients and healthy controls (p = 0.524 for the right olfactory nerve, p = 0.093 for the left)

n-CSF like

Among COVID-19 patients with anosmia the mean olfactory nerve n-CSF like value was 0.264 ± 0.149 on the right and 0.254 ± 0.103 on the left. Among healthy controls the mean olfactory nerve n-CSF like value was 0.239 ± 0.141 on the right and 0.250 ± 0.134 on the left. No significant difference was found between patients and healthy controls (p = 0.264 for the right olfactory nerve, p = 0.282 for the left).

n-GM like

Among COVID-19 patients with anosmia the mean olfactory nerve n-GM like value was 0.231 ± 0.170 on the right and 0.226 ± 0.130 on the left. Among healthy controls the mean olfactory nerve n-GM like value was 0.251 ± 0.181 on the right and 0.239 ± 0.135 on the left. No significant difference was found between patients and healthy controls (p = 0.119 for the right olfactory nerve, p = 0.977 for the left).

n-WM like

Among COVID-19 patients with anosmia the mean olfactory nerve n-WM like value was 0.200 ± 0.135 on the right and 0.195 ± 0.143 on the left. Among healthy controls the mean olfactory nerve n-WM like value was 0.187 ± 0.128 on the right and 0.174 ± 0.108 on the left. No significant difference was found between patients and healthy controls (p = 0.843 for the right olfactory nerve, p = 0.550 for the left).

**Table 1.** Comparison between DTI metrics in post-COVID-19 persistent hyposmia patients and healthy controls.

| | | Patients (N = 23) | Healthy Controls (N =37) | |
|---|---|---|---|---|
| **Metric** | **Side** | **m ± sd** | **m ± sd** | **p (Student's t test)** |
| MD (x $10^{-3}$ mm2/s) | right | 1.17 ± 0.36 | 1.21 ± 0.33 | 0.670 |
| | left | 1.13 ± 0.29 | 1.23 ± 0.26 | 0.195 |
| FA | right | 0.231 ± 0.049 | 0.223 ± 0.046 | 0.524 |
| | left | 0.239 ± 0.058 | 0.215 ± 0.049 | 0.093 |
| n-CSF like | right | 0.264 ± 0.149 | 0.239 ± 0.141 | 0.264 |
| | left | 0.254 ± 0.103 | 0.250 ± 0.134 | 0.282 |
| n-GM like | right | 0.231 ± 0.170 | 0.251 ± 0.181 | 0.119 |
| | left | 0.226 ± 0.130 | 0.239 ± 0.135 | 0.977 |
| n-WM like | right | 0.200 ± 0.135 | 0.187 ± 0.128 | 0.843 |
| | left | 0.195 ± 0.143 | 0.174 ± 0.108 | 0.550 |

**Discussion**

In our study, we were able to successfully reconstruct CN I in 23 post-COVID-19 patients with persistent hyposmia using a whole brain DTI multi-shell acquisition. The absence of microstructural alterations in patients in comparison to normal controls may have a two-fold explanation. Firstly, we cannot exclude the presence of contamination of air in the sinus cavities that may have introduced some variability, as suggested in previous studies attempting to reconstruct CN I (Echevarria-Cooper, Zhou et al. 2022). However, our negative results in terms of microstructural alterations are in line with a previous systematic review that failed to find morphological alterations in OBs in COVID-19 patients (Mohammadi, Gouravani et al. 2022) and may be in line with a recent large study published in Nature in which Douaud et al. showed that subjects with previous COVID-19 (n=401) had significantly greater atrophy cortical areas (i.e. orbitofrontal cortex and parahippocampal gyrus connected to primary olfactory cortices, as well as eduction in global brain compared with pre-infection findings and controls (n=384) (Douaud, Lee et al. 2022). Although in the second study the olfactory function was not investigated, evidence may suggest a central cortical mechanism supporting the development of persistent hyposmia in post-covid patients rather than a persistent microstructural alteration within the WM tract of CN I.

# Anterior optic pathway deformity in patients with sellar/parasellar tumors

## Introduction

The anatomical visualization of the anterior optic pathway, including the chiasm, using DTT has attracted great interest among neurosurgeons dealing with neoplasms of the sellar and parasellar regions, (e.g., pituitary adenomas, tuberculum sellae meningioma, craniopharyngiomas) that may cause extrinsic compression of the anterior visual pathway fibers when extending superiorly (Ma, Su et al. 2016). Surgical resection of these tumors is challenging due to the high potential for damage to the visual system. There is poor correlation between tumor extent on conventional MRI modalities and visual impairment (He, Zhang et al. 2021); therefore, detailed information about the fiber pathways and microstructural integrity could support in treatment decision-making and surgical planning and potentially improve clinical outcomes.

From a radiological point of view, optimal visualization of the CNs can be carried out using a variety of MRI sequences particularly employing steady-state acquisition sequences and constructive interference in steady-state sequences, especially using 3T MRI scanner (Mikami, Minamida et al. 2005). These types of studies provide excellent visualization of CN structures in two dimensions; however, they lack adequate measures of tract continuity and integrity. Furthermore, the three-dimensional relationship with surrounding structures cannot be immediately derived from these images.

Recent advances in DTI tractography have allowed for the use of this technique even in small (0.1-2 mm) structures outside of the brain parenchyma. In particular, there has been a great interest in CN depiction using DTI tractography, as reported in multiple publications in recent years (see “Previous Tractography Studies of Cranial Nerves” section for details). In fact, only DTI tractography can track *in vivo* the complex trajectory of CN fibers in the three dimensions and visualize structures not visible in conventional MRI (Puzniak, Ahmadi et al. 2019).

An important ongoing issue of CN tractography regards the validation of the anatomical accuracy of the reconstructions, which is still not defined. Although attempts have been made to establish a quantitative method of measuring the anatomical fidelity of the reconstructions, such as the computation of the Dice similarity coefficient between the tractographical reconstructions and a conventional MRI image (Zolal, Sobottka et al. 2017) or the normalized overlap score (NOS) between multiple reconstructions (He, Zhang et al. 2021), to date there is still no established method usable to separate the fibers that correspond to the CN from those that do not. Therefore, operator judgement continues to be extensively used. The claims that the position of the CN was detected using DTI tend to be somewhat questionable, because the decision about which reconstructions are accurate is made in a qualitative manner by the operator.

Some previous studies have reported the feasibility of performing CN tractography of anterior optic pathways tracts in some large (n = 62) (Jacquesson, Cotton et al. 2019), and small case series (n = 5) of patients with brain tumors (Ma, Su et al. 2016). Interestingly, in a 2015 World Neurosurgery article, Hajiabadi et al. (Hajiabadi, Alimohamadi et al. 2015) reported two patients with pituitary macroadenomas in which it was impossible to reconstruct the optic chiasma with DTI tractography preoperatively due to severe dislocation and compression but after surgery the reconstruction became possible along with improvement of the visual deficit. The authors suggested that the compression caused disturbance of axoplasmic flow and, therefore, the non-visualization of decussating chiasmatic fibers in DTI tractography.

Other studies have explored the possibility that DTI metrics within the reconstructed anterior tracts could correlate with clinical manifestations in patients with tumors of the sella turcica compressing the chiasm, and most referred to DTI metrics within the optic tracts. In particular, Paul at al. (Paul, Gaffin-Cahn et al. 2014) and Liang et al. (Liang, Lin et al. 2021) observed that DTI metrics within the optic tracts correlate with the degree of the visual deficit at the time of examination. Anik et al. (Anik, Anik et al. 2011) were the only group to report that the DTI metrics within the chiasm, particularly FA values below 0.4 and MD values over $1.400 \times 10^{-3}$ $mm^2$ $s^{-1}$, were associated with a lack of improvement in visual deficit at six-month follow-up.

On the other hand, Raz et al. (Raz, Bick et al. 2015) described a single patient who experienced an improvement of a bilateral bi-temporal vision reduction despite the presence of abnormal FA values within the optic tracts. The authors interpret their data as highlighting the ability of the remaining normally conductive axons to predict visual recovery following decompression of the optic chiasm, stating that this threshold effect may be related to the redundancy in the anterior visual pathway, which can be explained neuro-anatomically by overlapping receptive fields.

**Aim**

The primary aim of the current study was to assess the feasibility of a novel advanced DTI tractography pipeline including multi-shell DTI and probabilistic tractography reconstruction of the anterior optic pathway in patients with sellar/parasellar tumors. The second aim of the study was to explore the correlations between DTI metrics within various anterior optic pathway sections (i.e., right and left optic nerves, optic chiasm, and right and left optic tracts) and clinical data (i.e., presence of visual deficit and follow-up after surgery).

## Methods

### Study population

We included all consecutive patients with occupying lesions of the sella turcica/parasellar region with evidence of chiasmal compression who were candidates for endoscopic endonasal surgery in the Pituitary Unit at IRCSS Istituto delle Scienze Neurologiche di Bologna between May 2021 and August 2022. A group of sex- and age-matched healthy controls were selected from the Neuroimaging Laboratory at IRCSS Istituto delle Scienze Neurologiche di Bologna, designed to collect non-pathological MRI exams for clinical and research purposes. Written informed consent was obtained from all participants prior participation to the study which was conducted according to the Declaration of Helsinki guidelines and approved by the local ethic committee (Codice CE 815-2020-SPER-AUSLBO).

### Clinical evaluation

All patients were clinically assessed at baseline by an expert neurosurgeon who performed the neurological physical examination including the subjective visual field examination. In this examination the patient is asked to look directly at an object in front of him or her (such as the physician's nose), while one eye is covered. The neurosurgeon then moves his hand out of the patient's visual field and gradually brings it back in. The patient reports to the neurosurgeon when their hand comes back into view. Afterwards, all patients performed a computerized visual field examination and an ophthalmological examination to determine visual acuity. At these tests, bitemporal hemianopsia is defined as the loss of vision in the outer half of both the right and left visual fields and can be partial or complete. Right or left hemianopsia is defined as visual field loss on the left or right side of the vertical midline. This visual examination was repeated at six-month follow-up. Moreover, a complete evaluation of pituitary function (including measurement of blood levels of GH, IGF-1, PRL, LH, FSH, ACTH and ADH) was performed before surgery and at six-month follow-up. After surgery, pathological examination of the resected lesion was performed, and after six months clinical and endocrinological evaluations were repeated as part of the routine follow-up.

### MRI acquisition

*MRI specifications*

Images were acquired using a 3T MRI Scanner (Magnetom Skyra, Siemens, Erlagen, Germany) and VE11C-SP01 software (maximum gradient amplitude 45 mT/m; maximum "slew rate" 200 T/m/s) and a 64-channel phased head coil at the IRCSS Istituto delle Scienze Neurologiche di Bologna – Ospedale Bellaria, Bologna.

*Subject preparation*

Written informed consent was obtained from each participant before MRI examination. Participant removed all metallic or non-MRI compatible object before being positioned on the scanner bed in a head-first supine position. Participants were instructed to abstain from rotating their heads inside the coil. Head position was further restricted using foam pads. They used phono-absorbent earplugs to protect their ears from the high noise level. They were also given a bell to ring in case of emergency. The receiver coil has a mirror that allows the patient to see the control room and reduce the effect of claustrophobia.

*Scan protocol*

A standardized scan protocol was followed in which the following sequences were administered.

T1-weighted images acquired using a three-dimensional inversion recovery prepared spoiled gradient-echo (3D MPRAGE) sequence (flip angle = 9°; TI = 900 ms; TE = 2.98 ms; TR = 2300 ms; acquired matrix size = 256 × 256 × 256; phase FoV = 100%; reconstructed voxel size = 1 mm isotropic) were used as an anatomical reference.

The next sequence was a DTI multi-shell acquisition which employed a single-shot spin-echo EPI sequence with two different phase encoding directions (to better average the useful signal and eddy currents), A-P and P-A (TE = 98 ms; TR = 4300 ms; 87 contiguous 2-mm thick slices; FoV = 220 × 220 mm; acquired matrix = 110 x 110; reconstructed in-plane resolution = 2.0 mm) with diffusion sensitizing gradients applied in 131 (A-P) and 49 (P-A) non-collinear directions, 8 b = 0 s/mm$^2$ (A-P and P-A), 12 b = 300 s/mm$^2$ (A-P and P-A), 30 b = 1000 s/mm$^2$ (A-P and P-A), 64 b = 2000 s/mm$^2$ (A-P) volumes.

T2-weighted fluid-attenuated inversion recovery (FLAIR) images were acquired using an inversion recovery prepared fast spin echo sequence (flip angle = variable; TI = 1800 ms; TE = 428 ms; TR = 5000 ms; 176 contiguous 1-mm thick slices, FoV = 256 × 256 mm; reconstructed voxel size = 1 × 1 mm).

Next, T1-weighted coronal turbo spin echo (TSE) sequences were acquired centered on the sellar region (flip angle = 150; TE = 8.1 ms; TR = 650 ms; 15 contiguous 2-mm thick slices, FoV = 150 × 150 mm; reconstructed voxel size = 0.4 x 0.4 × 2 mm).

T2-weighted coronal TSE sequences were acquired centered on the sellar region (flip angle = 150°; TE = 99 ms; TR = 4000 ms; 13 contiguous 2-mm thick slices, FoV = 150 × 150 mm; reconstructed voxel size = 0.6 × 0.6 × 2 mm).

Lastly, T1-weighted sagittal TSE sequences were acquired centered on the sellar region [flip angle = 147°; TE = 8.8 ms; TR = 500 ms; 25 contiguous 2-mm thick slices, FoV = 150 × 150 mm; reconstructed voxel size = 0.8 × 0.8 × 2 mm].

At this point paramagnetic contrast agent (Gadoteridol 0.2 cc/kg) was administered to the patient intravenously, and the following acquisitions were repeated: coronal T1-weighted coronal TSE, sagittal T1-weighted coronal TSE, and 3D MPRAGE T1-weighted.

**Diffusion tensor tractography tract estimation**

*Imaging preprocessing*

Data from each participant were preprocessed using an in-house automated pipeline developed from software packages freely available as part of the Oxford FSL, version 6; the NIH AFNI, version 20.3.02; and MRtrix, version 3.0.2. The image format used was compressed NIfTI-1, extension ".nii.gz" ("NIfTI-1 Data Format").

DW images were skull-stripped using the FSL "bet" tool. Image denoising was performed with the MRtrix3 "dwidenoise" function (Veraart, Novikov et al. 2016), implementing a principal component analysis approach. Susceptibility-related distortions in the EPI acquisition were estimated using the FSL "topup" function; subsequently, a combined correction for susceptibility, eddy-current effects, and signal dropout, most commonly induced by subject movement, was performed by FSL "eddy_openmp," based on the "topup" estimates.

The DWI data were modelled at the voxel level using functions of the MRtrix toolkit. In particular, the response function for SD was modelled using the "Dhollander" algorithm within "dwi2response" (Dhollander, Mito et al. 2019). FODs were estimated using multi-shell multi-tissue SD using the "msmt_csd" method implemented in the "dwi2fod" function (Jeurissen, Tournier et al. 2014), as described in Manners et al. (Manners, Gramegna et al. 2022).

Characterization of the diffusion properties of tissue within each voxel was provided by FSL "dtifit" based on the diffusion tensor, which was used to estimate voxel FA and MD.

*Tract estimation*

The MRtrix tool "tckgen" generated these streamlines by an iFOD1 approach (Tournier, Calamante et al. 2012), following the procedure described by He et al. (He, Zhang et al. 2021).

In order to isolate the anterior optic pathway, selected fibers were transformed to the NIfTI format to create a volumetric probability map based on fiber density. Voxels were subjected to a threshold that excluded low probability tracts as detailed in the following section.

**Anterior optic pathway reconstruction**

*Processing*

On the MNI152 standard brain, a mask including the trajectory of the entire anterior optic pathway from the optic bulb to the LGN (called "NERVO_mask") was drawn. A single automatic exclusion ROI including all the possible spurious segment originating from the principal tract (called "ROI_NERVO_excl") was then created. Next, a seed from LGN ("ROI_II_LGN"), an inclusion ROI in the optic chiasm ("ROI_II_chiasm") and a target ("ROI_II_orbit") were drawn.

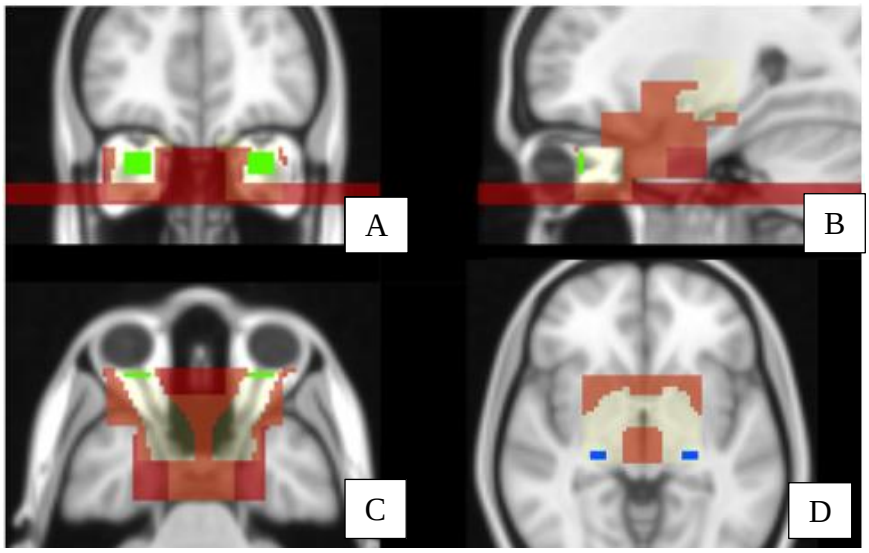


**Figure 2.** Coronal (A), sagittal (B), and axial (C-D) reconstruction of the study template for CN II reconstruction. In yellow: the mask including all the trajectory of the whole anterior optic pathway from the optic bulb to the lateral geniculate nucleus. An automatic exclusion region of interest including all the possible spurious segment originating from the principal tract was then created (in red). Finally, seeds from the lateral geniculate nucleus in blue and one in the orbit were drawn.

A linear-affine registration was performed between the $b_0$ image of the DTI and the 3D MPRAGE T1 using the "flirt" tool in FSL, and one non-linear (using "fnirt" of FSL) between the 3D MPRAGE T1 and the MNI, in order to achieve an indirect transformation between the $b_0$ image and MNI. This registration is applied to each ROI with the "applywarp" function (using the "nearest neighbour" approach for the mask and the exclusion and the "trilinear approach" for the others). For each hemisphere (Left = L and Right = R), the iFOD1 ("tckgen") method was applied to generate up to 5,000,000 streamlines from the LGN ROI (seed), then selecting only those fulfilling specified criteria: angle ≤ 10°, cutoff/seed_cutoff = 0.005, crossing the ROI of the chiasma and reaching the ipsilateral or contralateral ROI of the orbit (target). The seeding eventually stopped if 1000 were selected according to the above constraints. As a result, the four possible combinations of crossing (LR, RL) or non-crossing (LL, RR) tracks were separately reconstructed. The same procedure was repeated after inverting the seed and the target and the pairs of corresponding tracks by seed and target were added into a single tract. The tracts were then transformed into an image in the NIfTI format, where the voxel intensity was proportional to the density of the streamlines; lastly, a threshold set at 10% of the maximum value was applied to obtain the "final_nifti".

*Transfer to the neuronavigation system*

In order to transfer the images to the neuronavigator system (StealthStation S7 MEDTRONIC, Louisville, CO, US), each anterior optic pathway reconstruction was registered from the $b_0$ image of the DTI to the 3D MPRAGE T1 using a trilinear interpolation and subjected to a threshold set at 15% of the maximum, after which the image was binarized and superimposed on the 3D MPRAGE T1. The resulting images were visualized by the neuroradiologist, and a higher threshold was selected if needed, and the NIfTI image was transformed to a Digital Imaging and Communications in Medicine (DICOM) format using the free Karawun python package https://github.com/DevelopmentalImagingMCRI/karawun.

*Along-tract analysis*

In order to perform the along-tract analysis, the "final_nifti" file was used to mask each of the streamline file defining the four tracks (Left geniculate – Left orbit track; Left geniculate – Right orbit track, Right geniculate – Left orbit track, Right geniculate _ Right orbit track). For each of these tracks, the streamline file was registered to the MNI using the "tcktransform" option. For each tract, the most extreme points ware defined as the most extremal points that ware reached by at least 50% of the fibers in the anterior and posterior directions. To identify them, the nerve was cut in each slice of the NIfTI image in the main direction of the nerve (typically the y-axis) and the number of streamlines passing through each slice was calculated using the "tckedit + tckstats" option of MRtrix. (Tournier, Smith, Ret al. 2019). The two identified extremal points of each track define a line, which iwa used to do the resampling (using the "tckresample" function) of each line in 15 equidistant points.

Segments 1-7 are those corresponding to the optic tract, segments 7-9 to the optic chiasm, and segments 10-15 to the optic nerves.

**DTI metrics definition**

For each of these points the DTI-derived metrics, MD and FA were calculated and averaged for the right and left optic nerve, optic chiasm, and optic tracts. Moreover, since FODs were estimated using multi-shell multi-tissue SD models we were able to infer three parameters from three tissue compartments: two with isotropic diffusion characteristics, one representing restricted diffusion and labelled GM and the other representing unhindered diffusion and labelled CSF; finally one component with anisotropic characteristics modelled as a tensor, labelled WM (Manners, Gramegna et al. 2022).

**Neuroradiological confirmation**

The reconstructed tracts were superimposed on a 3D MPRAGE T1 image and visualized by an expert neuroradiologist. In cases of patients for whom the algorithm failed to automatically reconstruct the pathway, a manual optic chiasm ROI was drawn and the algorithm performed again. If the algorithm failed again, a secondary exclusion ROI in/near the tumor was used as exclusion mask.

**Surgical confirmation**

All patients underwent an endoscopic endonasal approach utilizing neuronavigation, with a goal of complete resection. In a subgroup of patients, the DTI three-dimensional reconstruction images were transformed into DICOM format and transferred to the neuronavigation system with dedicated software for endoscopic procedures (StealthStation S8, Medtronic, Louisville, CO, USA). For each patient, the reconstruction adherence of the tracking (evaluated at the neuronavigation) to the intraoperative identification of the optic structures and evaluated as fully compliant (Jacquesson, Cotton et al. 2019).

**Statistical analysis**

Continuous variables are expressed as mean and standard deviation (SD), while categorical variables are expressed by absolute numbers (n) and percentages (%). Groups were compared using Student's t-test or Mann-Whitney U test, as appropriate, for continuous variables and Pearson chi-square test or Fisher's exact test, as appropriate, for categorical variables.

DTI metrics were compared between patients (whole group, patients presenting with visual symptoms, patients presenting with bitemporal hemianopia) and controls using an unpaired two-sided t-test. Patients presenting with visual symptoms were divided between those who experienced complete resolution of symptoms ("responders") and those who did not ("non-responders") at six months follow-up and un unpaired t-test was performed to compare these responders vs non responders.

## Results

### Study population

A total of 27 patients with sellar/parasellar tumors displacing the optic chiasm were included (13 female, mean age: 53.3 ± 16.4 years).

### Pathological and molecular sellar lesion diagnosis

Based upon pathological examination, 20/27 (74.1%) patients had pituitary macroadenomas; among these, 13 cases were diagnosed as gonadotropinomas, three cases as plurihormonal PIT-1 positive adenomas, three cases as silent corticotropinomas, and one case as a mixed somatotroph-lactotroph adenoma.

Of the remaining seven cases, three (11.1%) were meningiomas (WHO grade 1), two (7.4%) were craniopharyngiomas, and two (7.4%) were other diagnoses such as pilocytic astrocytoma and mature teratoma.

Pituitary function was assessed to be normal in 23/27 (85.2%) patients except three who presented with anterior hypopituitarism and one with panhypopituitarism. Three patients with macroadenomas presented clinical evidence of hormonal hypersecretion; specifically, two patients showed high plasmatic levels of prolactin (PRL) and one showed high plasmatic levels of growth hormone/insulin-like growth factor -1 (GH/IGF-1).

### Visual deficit

Twenty out of 27 patients (74.1%) presented visual symptoms, and among them 13 (65%) displayed temporal hemianopsia, four (20%) showed a left hemianopsia, and three (15%) had right hemianopsia.

### Clinical and endocrinological follow-up

At six-month follow-up, nine out of 27 patients (33.3%) presented abnormal pituitary function. Upon clinical examination, seven out of 20 patients (35%) presented a resolution of visual symptoms whereas 13 (65%) showed a partial resolution.

### Neuroradiological confirmation

All the 3D MPRAGE T1 images were considered of good quality, the three-dimensional tractographic reconstruction were superimposed on the 3D MPRAGE T1 and visually evaluated by an expert neuroradiologist. During neuroradiological examination, the tractography algorithm was judge to fully automatically perform the tractographical reconstruction in 16/27 (59.3%), in 11/27 (40.27%) cases it was necessary to add a manual chiasm ROI, the algorithm was performed again and then able to reconstruct the anterior optic pathway in all patients.

In all but five patients (22/27, 81.5%) all five tracts (right optic nerve, left optic nerve, chiasm, right optic tract, left optic tract) were correctly reconstructed, for a total of 130/135 (96.3%) tracts reconstructed.

**Figure 3.** Reconstruction of the optic chiasm in patient with macroadenoma.

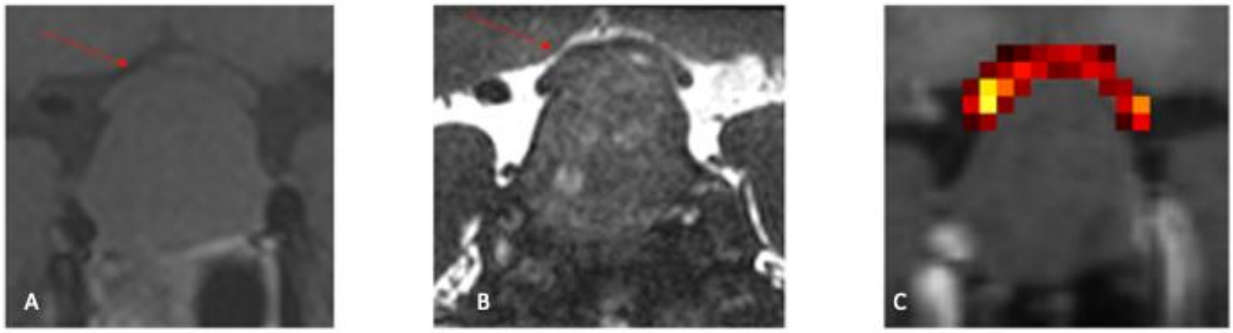


Legend: A. Coronal turbo spin echo image and B. coronal constructive interference in steady state reconstruction showing upwards displacement of the optic chiasm (red arrow), which was successfully reconstructed by the fractographic algorithm and superimposed on the 3D MPRAGE T1 image (C) in a patient with macroadenoma (gonadotropinoma).

**Figure 4.** Reconstruction of the optic nerve and chiasm in patient with pilocytic astrocytoma

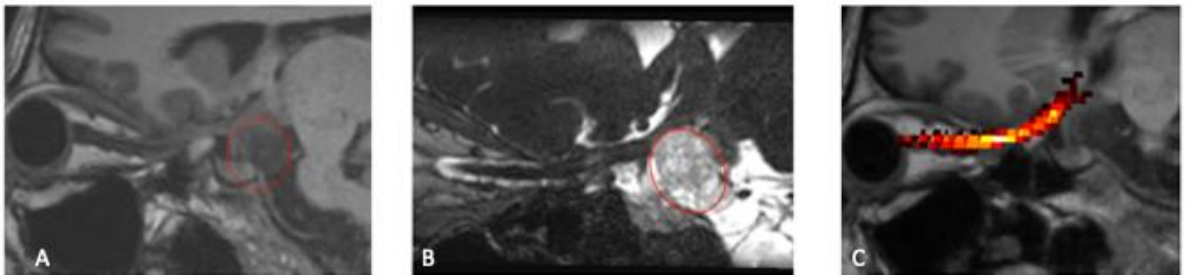


Legend: A. Sagittal 3D MPRAGE T1 and B. sagittal constructive interference in steady state reconstruction showing a pilocytic astrocytoma (red circle) in which the optic nerve and chiasm were successfully reconstructed and superimposed on the sagittal 3D MPRAGE T1 (C).

**Figure 5.** Reconstruction of the optic nerve and chiasm in patient with mature teratoma

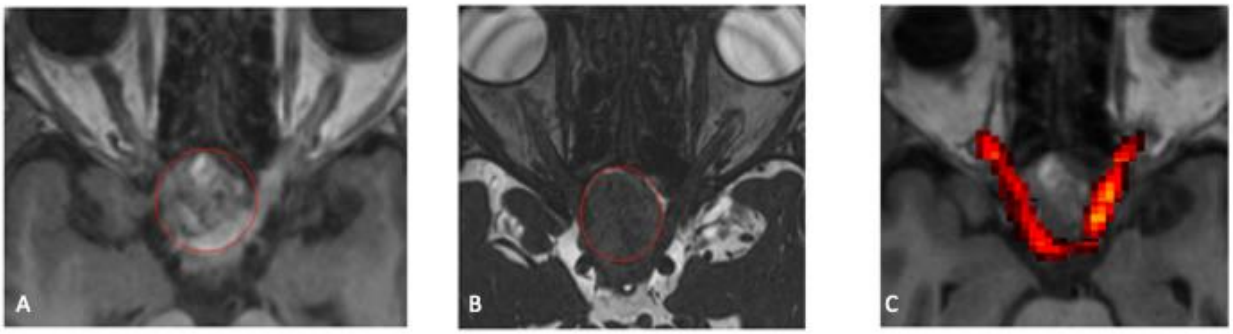

Legend: A. Axial 3D MPRAGE T1 and B. axial constructive interference in steady state reconstruction showing a patients with mature teratoma (red circle) in which the optic nerve and chiasm were successfully reconstructed and superimposed on the axial 3D MPRAGE T1 (C).

**Neurosurgical confirmation**

Upon visual inspection during surgery in 13 patients, all but two patients (11/13, 84.7%) presented a correct correspondence of all segments. In two patients, it was impossible to confirm the presence of both optic tracts, resulting in a total of 61/65 (81.3%) tracts surgically confirmed.

**DTI Metrics results**

Significant and no significant difference in DTI metrics in patients with sellar/parasellar tumors and healthy controls are reported in **Table 2**. Comparisons between patients with visual deficit and without, and patients with temporal hemianopsia and without, are reported in **Table 3** and **Table 4**. Comparisons between responders and non-responders are reported in **Table 4**.

**Table 2.** DTI metrics in patients with sellar/parasellar tumors and healthy controls.

| | | Patients (N = 27) | | Healthy Controls (N = 30) | | |
|---|---|---|---|---|---|---|
| **Structure** | **Metric** | **m ± sd** | **min - max** | **m ± sd** | **min - max** | **p (t)** |
| **Right optic nerve** | MD ($\mu m^2/s$) | 1.43 ± 0.29 | 0.95 – 2.37 | 1.37 ± 0.22 | 0.89 – 1.78 | 0.375 |
| | **FA** | 0.301 ± 0.068 | 0.161 – 0.464 | 0.339 ± 0.048 | 0.266 – 0.464 | **0.018** |
| | nCSF-like | 0.173 ± 0.064 | 0.084 – 0.413 | 0.184 ± 0.084 | 0.063 – 0.462 | 0.606 |
| | nGM-like | 0.187 ± 0.063 | 0.073 – 0.342 | 0.172 ± 0.092 | 0.056 – 0.462 | 0.497 |
| | **nWM-like** | 0.257 ± 0.069 | 0.107 – 0.400 | 0.306 ± 0.072 | 0.163 – 0.462 | **0.014** |
| **Left optic nerve** | **MD ($\mu m^2/s$)** | 1.45 ± 0.27 | 1.04 – 2.04 | 1.51 ± 0.20 | 1.09 – 1.87 | 0.362 |
| | FA | 0.322 ± 0.063 | 0.189 – 0.473 | 0.327 ± 0.055 | 0.196 – 0.456 | 0.760 |
| | **nCSF-like** | 0.172 ± 0.063 | 0.089 – 0.367 | 0.210 ± 0.068 | 0.110 – 0.435 | **0.033** |
| | nGM-like | 0.191 ± 0.066 | 0.083 – 0.322 | 0.178 ± 0.090 | 0.062 – 0.435 | 0.544 |
| | **nWM-like** | 0.260 ± 0.079 | 0.130 – 0.402 | 0.321 ± 0.089 | 0.087 – 0.492 | **0.009** |
| **Optic chiasm** | MD ($\mu m^2/s$) | 1.75 ± 0.25 | 1.31 – 2.30 | 2.13 ± 0.23 | 1.49 – 2.55 | **< 0.001** |
| | FA | 0.239 ± 0.044 | 0.124 – 0.337 | 0.248 ± 0.058 | 0.156 – 0.450 | 0.518 |
| | **nCSF-like** | 0.308 ± 0.077 | 0.176 – 0.501 | 0.448 ± 0.083 | 0.272 – 0.645 | **< 0.001** |
| | **nGM-like** | 0.247 ± 0.080 | 0.095 – 0.411 | 0.168 ± 0.085 | 0.069 – 0.450 | **0.001** |
| | **nWM-like** | 0.393 ± 0.094 | 0.210 – 0.553 | 0.329 ± 0.077 | 0.192 – 0.496 | **0.007** |
| **Right optic tract** | **MD** ($\mu m^2/s$) | 1.41 ± 0.21 | 1.15 – 2.07 | 1.29 ± 0.09 | 1.07 – 1.43 | **0.007** |
| | **FA** | 0.407 ± 0.081 | 0.148 – 0.542 | 0.468 ± 0.053 | 0.301 – 0.554 | **0.001** |
| | nCSF-like | 0.187 ± 0.055 | 0.113 – 0.351 | 0.173 ± 0.072 | 0.90 – 0.433 | 0.428 |
| | **nGM-like** | 0.251 ± 0.118 | 0.077 – 0.497 | 0.188 ± 0.069 | 0.098 – 0.433 | **0.017** |
| | **nWM-like** | 0.554 ± 0.132 | 0.298 – 0.779 | 0.632 ± 0.113 | 0.301 – 0.766 | **0.022** |
| **Left optic tract** | **MD** ($\mu m^2/s$) | 1.34 ± 0.16 | 1.10 – 1.62 | 1.26 ± 0.09 | 1.13 – 1.54 | **0.024** |
| | **FA** | 0.430 ± 0.076 | 0.216 – 0.539 | 0.477 ± 0.057 | 0.309 – 0.571 | **0.011** |
| | nCSF-like | 0.168 ± 0.054 | 0.080 – 0.318 | 0.162 – 0.075 | 0.090 – 0.412 | 0.731 |
| | **nGM-like** | 0.243 ± 0.098 | 0.087 – 0.489 | 0.194 ± 0.068 | 0.087 – 0.412 | **0.030** |
| | nWM-like | 0.581 ± 0.122 | 0.354 – 0.785 | 0.636 ± 0.120 | 0.309 – 0.784 | 0.095 |

*Patients with visual deficits*

The differences in the DTI metrics of patients with sellar and parasellar tumors who presented visual symptoms were in comparison to those who not presented visual deficit are reported in the table below. The only statistically significant difference was found between patients with visual symptoms and those without in the left optic nerve (p = 0.027).

**Table 3.** DTI metrics in patients with and without visual symptoms

| | | **Patients with visual symptoms** | | **Patients without visual symptoms** | | |
|---|---|---|---|---|---|---|
| **Structure** | **Metric** | **m ± sd** | **min - max** | **m ± sd** | **min - max** | **p (t)** |
| **Right optic nerve** | MD ($\mu m^2/s$) | 1.38 ± 0.32 | 9.5 – 2.37 | 1.54 ± 0.19 | 1.34 – 1.87 | 0.244 |
| | **FA** | 0.303 ± 0.078 | 0.161 – 0.464 | 0.308 ± 0.057 | 0.257 – 0.417 | 0.865 |
| | nCSF-like | 0.167 ± 0.070 | 0.084 – 0.413 | 0.186 ± 0.050 | 0.123 – 0.257 | 0.456 |
| | nGM-like | 0.195 ± 0.063 | 0.090 – 0.342 | 0.165 ± 0.061 | 0.073 – 0.227 | 0.284 |
| | nWM-like | 0.247 ± 0.070 | 0.107 – 0.400 | 0.284 ± 0.062 | 0.217 – 0.367 | 0.235 |
| **Left optic nerve** | **MD ($\mu m^2/s$)** | 1.41 ± 0.27 | 1.04 – 2.04 | 1.53 ± 0.27 | 1.19 – 1.87 | 0.374 |
| | FA | 0.315 ± 0.059 | 0.189 – 0.404 | 0.345 ± 0.076 | 0.259 – 0.473 | 0.315 |
| | nCSF-like | 0.167 ± 0.066 | 0.089 – 0.367 | 0.178 ± 0.060 | 0.097 – 0.260 | 0.587 |
| | nGM-like | 0.206 ± 0.064 | 0.130 – 0.322 | 0.152 ± 0.058 | 0.083 – 0.251 | 0.062 |
| | **nWM-like** | 0.239 ± 0.083 | 0.130 – 0.402 | 0.315 ± 0.024 | 0.277 – 0.345 | 0.027 |
| **Optic chiasm** | MD ($\mu m^2/s$) | 1.72 ± 0.26 | 1.21 – 2.30 | 1.83 ± 0.20 | 1.55 – 2.10 | 0.317 |
| | FA | 0.253 ± 0.042 | 0.180 – 0.337 | 0.235 ± 0.032 | 0.181 – 0.278 | 0.324 |
| | nCSF-like | 0.300 ± 0.083 | 0.176 – 0.501 | 0.328 ± 0.058 | 0.243 – 0.397 | 0.346 |
| | nGM-like | 0.254 ± 0.073 | 0.141 – 0.411 | 0.229 ± 0.102 | 0.095 – 0.353 | 0.499 |
| | nWM-like | 0.401 ± 0.098 | 0.210 – 0.553 | 0.372 ± 0.085 | 0.234 – 0.487 | 0.508 |
| **Right optic tract** | MD ($\mu m^2/s$) | 1.42 ± 0.23 | 1.15 -2.07 | 1.35 ± 0.17 | 1.17 – 1.65 | 0.503 |
| | FA | 0.413 ± 0.059 | 0.296 – 0.498 | 0.453 ± 0.062 | 0.350 – 0.542 | 0.180 |
| | nCSF-like | 0.193 ± 0.054 | 0.113 – 0.351 | 0.146 ± 0.024 | 0.120 – 0.184 | 0.353 |
| | nGM-like | 0.275 ± 0.121 | 0.080 – 0.497 | 0.175 ± 0.073 | 0.077 – 0.300 | 0.070 |
| | nWM-like | 0.526 ± 0.127 | 0.298 – 0.763 | 0.641 ± 0.120 | 0.417 – 0.779 | 0.062 |
| **Left optic tract** | MD ($\mu m^2/s$) | 1.37 ± 0.15 | 1.20 – 1.62 | 1.27 ± 0.16 | 1.10 – 1.61 | 0.170 |
| | FA | 0.419 ± 0.080 | 0.216 – 0.539 | 0.474 ± 0.046 | 0.390 – 0.536 | 0.353 |
| | nCSF-like | 0.178 ± 0.049 | 0.112 – 0.318 | 0.122 ± 0.027 | 0.080 – 0.152 | 0.128 |
| | nGM-like | 0.260 ± 0.105 | 0.093 – 0.489 | 0.198 ± 0.060 | 0.087 – 0.268 | 0.159 |
| | nWM-like | 0.556 ± 0.120 | 0.354 – 0.785 | 0.648 ± 0.109 | 0.432 – 0.760 | 0.089 |

*Patients with bitemporal hemianopia*

The differences in the DTI metrics of patients with sellar and parasellar tumors who presented with bitemporal hemianopsia in comparison to those who presented with other temporal deficits are presented below.

**Table 4.** DTI metrics in patients with and without bitemporal hemianopsia

| | | **Patients with bitemporal hemianopsia** | | **Patients without bitemporal hemianopsia** | | |
|---|---|---|---|---|---|---|
| **Structure** | **Metric** | **m ± sd** | **min – max** | **m ± sd** | **min – max** | **p (t)** |
| Right optic nerve | MD ($\mu m^2/s$) | 1.34 ± 0.20 | 0.95 – 1.55 | 1.45 ± 0.47 | 1.02 – 2.37 | 0.534 |
| | **FA** | 0.304 ± 0.066 | 0.224 – 0.417 | 0.287 ± 0.101 | 0.161 – 0.464 | 0.695 |
| | nCSF-like | 0.152 ± 0.032 | 0.100 – 0.204 | 0.189 ± 0.105 | 0.084 – 0.413 | 0.271 |
| | nGM-like | 0.208 ± 0.066 | 0.129 – 0.342 | 0.182 ± 0.064 | 0.090 – 0.288 | 0.425 |
| | **nWM-like** | 0.259 ± 0.058 | 0.191 – 0.400 | 0.229 ± 0.088 | 0.107 – 0.347 | 0.401 |
| Left optic nerve | **MD ($\mu m^2/s$)** | 1.40 ± 0.21 | 1.04-1.74 | 1.45 ± 0.36 | 1.04 – 2.04 | 0.730 |
| | FA | 0.316 ± 0.056 | 0.234 – 0.404 | 0.308 ± 0.066 | 0.189 – 0.377 | 0.804 |
| | **nCSF-like** | 0.159 ± 0.040 | 0.089 – 0.232 | 0.182 ± 0.097 | 0.090 – 0.367 | 0.456 |
| | nGM-like | 0.212 ± 0.071 | 0.130 – 0.322 | 0.283 ± 0.075 | 0.136 – 0.304 | 0.757 |
| | **nWM-like** | 0.240 ± 0.074 | 0.146 – 0.402 | 0.237 ± 0.102 | 0.130 – 0.360 | 0.944 |
| Optic chiasm | MD ($\mu m^2/s$) | 1.71 ± 0.31 | 1.31 – 2.30 | 1.73 ± 0.20 | 1.44 – 1.99 | 0.915 |
| | FA | 0.251 ± 0.046 | 0.180 – 0.337 | 0.251 ± 0.033 | 0.212 – 0.289 | 0.989 |
| | nCSF-like | 0.284 ± 0.084 | 0.176 – 0.501 | 0.318 ± 0.089 | 0.194 – 0.429 | 0.437 |
| | nGM-like | 0.246 ± 0.071 | 0.141 – 0.351 | 0.202 ± 0.061 | 0.181 – 0.411 | 0.321 |
| | nWM-like | 0.414 ± 0.081 | 0.319 – 0.538 | 0.372 ± 0.133 | 0.210 – 0.553 | 0.394 |
| Right optic tract | MD ($\mu m^2/s$) | 1.45 ± 0.29 | 1.15 – 2.07 | 1.39 ± 0.08 | 1.30 – 1.49 | 0.624 |
| | FA | 0.405 ± 0.074 | 0.296 – 0.498 | 0.416 ± 0.023 | 0.378 – 0.446 | 0.728 |
| | nCSF-like | 0.194 ± 0.057 | 0.113 – 0.351 | 0.189 ± 0.044 | 0.128 – 0.238 | 0.831 |
| | nGM-like | 0.259 ± 0.138 | 0.080 – 0.497 | 0.325 ± 0.068 | 0.224 – 0.420 | 0.289 |
| | nWM-like | 0.542 ± 0.138 | 0.298 – 0.763 | 0.492 ± 0.100 | 0.378 – 0.614 | 0.441 |
| Left optic tract | MD ($\mu m^2/s$) | 1.33 ± 0.15 | 1.20 – 1.62 | 1.42 ± 0.16 | 1.24 – 1.62 | 0.277 |
| | FA | 0.427 ± 0.090 | 0.216 – 0.539 | 0.398 ± 0.049 | 0.336 – 0.465 | 0.478 |
| | nCSF-like | 0.172 ± 0.037 | 0.122 – 0.234 | 0.188 ± 0.067 | 0.112 – 0.318 | 0.503 |
| | nGM-like | 0.227 ± 0.084 | 0.093 – 0.381 | 0.329 ± 0.105 | 0.157 – 0.489 | 0.036 |
| | nWM-like | 0.592 ± 0.106 | 0.397 – 0.785 | 0.496 ± 0.126 | 0.354 – 0.696 | 0.093 |

*Patients with different visual recovery*

The differences in the DTI metrics of patients with sellar and parasellar tumors who presented resolution of the visual symptoms in comparison to those who did not are presented below.

**Table 5.** DTI metrics in patients with and without visual improvement

| | | **Patients with visual improvement (N = 7)** | | **Patients without visual improvement (N = 13)** | | |
|---|---|---|---|---|---|---|
| **Structure** | **Metric** | **m ± sd** | **min – max** | **m ± sd** | **min – max** | **p (t)** |
| Right optic nerve | MD ($\mu m^2/s$) | 1.32 ± 0.14 | 1.12 – 1.55 | 1.44 ± 0.43 | 0.95 – 2.37 | 0.518 |
| | FA | 0.298 ± 0.062 | 0.235 – 0.417 | 0.296 ± 0.081 | 0.161 – 0.464 | 0.974 |
| | nCSF-like | 0.168 ± 0.044 | 0.112 – 0.257 | 0.174 ± 0.088 | 0.084 – 0.413 | 0.858 |
| | nGM-like | 0.199 ± 0.072 | 0.129 – 0.342 | 0.196 ± 0.058 | 0.090 – 0.288 | 0.297 |
| | nWM-like | 0.254 ± 0.066 | 0.148 – 0.367 | 0.253 ± 0.082 | 0.107 – 0.400 | 0.977 |
| Left optic nerve | MD ($\mu m^2/s$) | 1.25 ± 0.20 | 1.04 – 1.53 | 1.55 ± 0.24 | 1.22 – 2.04 | 0.019 |
| | FA | 0.318 ± 0.058 | 0.234 – 0.404 | 0.309 ± 0.055 | 0.189 – 0.377 | 0.746 |
| | nCSF-like | 0.147 ± 0.059 | 0.089 – 0.238 | 0.187 ± 0.068 | 0.105 – 0.367 | 0.197 |
| | nGM-like | 0.186 ± 0.068 | 0.130 – 0.304 | 0.224 ± 0.064 | 0.136 – 0.322 | 0.237 |
| | nWM-like | 0.239 ± 0.092 | 0.130 – 0.360 | 0.246 ± 0.080 | 0.146 – 0.402 | 0.861 |
| Optic chiasm | MD ($\mu m^2/s$) | 1.74 ± 0.20 | 1.44 – 2.30 | 1.70 ± 0.21 | 1.31 – 1.99 | 0.818 |
| | FA | 0.237 ± 0.027 | 0.210 – 0.277 | 0.240 ± 0.057 | 0.124 – 0.337 | 0.905 |
| | nCSF-like | 0.320 ± 0.122 | 0.176 – 0.501 | 0.290 ± 0.052 | 0.194 – 0.397 | 0.440 |
| | nGM-like | 0.228 ± 0.065 | 0.141 – 0.292 | 0.266 ± 0.075 | 0.174 – 0.411 | 0.299 |
| | nWM-like | 0.387 ± 0.113 | 0.274 – 0.553 | 0.400 ± 0.095 | 0.210 – 0.538 | 0.796 |
| Right optic tract | MD ($\mu m^2/s$) | 1.44 ± 0.29 | 1.26 – 2.07 | 1.41 ± 0.19 | 1.15 – 1.79 | 0.852 |
| | FA | 0.436 ± 0.046 | 0.337 – 0.483 | 0.369 ± 0.088 | 0.148 – 0.498 | 0.061 |
| | nCSF-like | 0.193 ± 0.072 | 0.128 – 0.351 | 0.189 ± 0.039 | 0.113 – 0.250 | 0.850 |
| | nGM-like | 0.223 ± 0.138 | 0.080 – 0.420 | 0.314 ± 0.105 | 0.116 – 0.497 | 0.113 |
| | nWM-like | 0.583 ± 0.113 | 0.383 – 0.705 | 0.500 ± 0.129 | 0.298 – 0.763 | 0.155 |
| Left optic tract | MD ($\mu m^2/s$) | 1.41 ± 0.17 | 1.20 – 1.62 | 1.34 ± 0.14 | 1.23 – 1.62 | 0.384 |
| | FA | 0.424 ± 0.105 | 0.216 – 0.536 | 0.417 ± 0.067 | 0.304 – 0.539 | 0.855 |
| | nCSF-like | 0.182 ± 0.070 | 0.080 – 0.318 | 0.167 ± 0.040 | 0.112 – 0.234 | 0.548 |
| | nGM-like | 0.248 ± 0.099 | 0.112 – 0.374 | 0.275 ± 0.111 | 0.093 – 0.489 | 0.606 |
| | nWM-like | 0.584 ± 0.138 | 0.388 – 0.760 | 0.555 ± 0.121 | 0.354 – 0.785 | 0.629 |

**Discussion**

In this part of my thesis I have presented the largest case series of sellar/parasellar tumors patients with a successful tractography reconstruction of the anterior optic pathway. We evaluated the anatomical fidelity of the reconstruction during surgery and explored the clinical significance of the metrics inside the tracts, finding a reduction in MD within the optic chiasm and a reduction of FA in the optic tracts of patients compared to healthy controls.

While Liang et al. (Liang, Lin et al. 2021) published a larger case series (n=65) of patients with pituitary tumors in which anterior optic tractography was performed, there is no mention in their study of the anatomical fidelity of tractography reconstruction. Moreover, the tractography was performed with a deterministic algorithm of diffusion spectrum images measuring the different degrees of anisotropy of the diffusion signal decay. Interestingly, the authors found a significant association between the anisotropic metrics in the optic nerve and tracts (the chiasm is not mentioned) and the degree of visual field defect. However, no data were reported on the association between the response to treatment in terms of the resolution of the visual symptoms after surgery and the DTI metrics.

One other previous ancillary DTI study published by Hajiabadi et al. in 2016 (Hajiabadi, Samii et al. 2016) reported that tractography reconstructed the anterior optic pathway in 22 (88%) of the 25 patients with pituitary tumors included. The authors reported that in those patients in whom the chiasm was impossible to reconstruct there was less visual improvement at three months follow-up. Finally, Anik et al. (Anik, Anik et al. 2011) performed a retrospective study including 72 patients with pituitary adenoma who had a preoperative DTI examination in which the anterior optic pathway tractography reconstruction was retrospectively performed. The method of validation of anatomical fidelity was not described; however, the authors assessed the optic chiasm by DTI, including each optic nerve nasal and temporal segments at the prechiasmatic portion, both sides, and central part of the chiasma, optic tract just after chiasma, and also the affected side of the nerves. A mean FA of 0.400 and MD values over $1.4\times10^{-6}$ $mm^2$ $s^{-1}$ were related with no visual improvement in the postoperative 6 months period. In none of the above-mentioned studies was the tractographic reconstruction used for presurgical planning.

Only two previous studies reported the use of tractographic reconstruction of the anterior optic pathway in the presurgical planning of patients. Yoshino et al. (Yoshino, Abhinav et al. 2016) reported the surgical confirmation of cranial nerve reconstruction in three patients. In particular, a 35-year-old woman with an optic-hypothalamic glioma in which a presurgical DTT study showed clear visualization of the optic nerves, optic chiasm, and optic tracts with predominant inferior displacement of the optic apparatus, obvious infiltration and damage of the right optic nerve, and lateral displacement of the left optic nerve. The imaging findings were considered critical in choosing the supraorbital over the endonasal approach. The second case was a 62-year-old woman with a petroclival meningioma in which preoperative DTI tracked CN III which was severely displaced superiorly and medially. The location of reconstructed CNs was consistent with the intraoperative findings. In the last patient, a 39-year-old male, a giant adenoma with a large

suprasellar extension and bilateral cavernous sinus invasion was studied. Preoperative DTT showed severe displacement of the optic chiasm in the superior and posterior directions which were confirmed intraoperatively.

In the large case series published by Jacquesson et al. (Jacquesson, Cotton et al. 2019) in which a total of 372 cranial nerves in 62 patients (the exact number and type of nerve for each patient is not specified in the study) were reported to be successfully tracked, among which 175 were considered to be displaced; only one patient was treated with endoscopic endonasal surgery for a sellar lesion, and in one other with a petroclival meningioma, the displacement of CN III changed the surgical approach from the endonasal to open surgery.

The interpretation of the increase in MD at the level of the displaced optic chiasm is interesting and challenging. A single previous animal study (Clifford-Jones, McDonald et al. 1985) was performed in which a chronic progressive compression of the optic nerve in a cat was produced by an inflatable silicon rubber balloon implanted in the orbit, simulating a chiasmal displacement. The authors found that within the first week the predominant pathological change was demyelination. Both partially and completely demyelinated fibers were seen at all stages of the experiments but by the fifth week, as some axons had been remyelinated by oligodendrocytes despite the continued presence of the balloon. The myelin sheaths of the new internodes were abnormally thin and short, and many showed an atypical paranodal organization. There was evidence of the breakdown of some of the new internodes. Given this evidence, one first speculative explanation for the reduction in MD may be associated to the phenomenon of re-myelinization and or glial activation at this level.

One other explanation may be associated with the presence of more leaflets of glia in the same space, due to the severe displacing of the structure in which more myelin sheets are concentrated in the same space, since it has been demonstrated that the length of the biological membrane is one of the independent predictors of ADC values in cellular models (Eida, Van Cauteren et al. 2016)

One potential reason for the absence of significant association of our metrics with clinical characteristics of the visual deficit may lie in the fact that patients with lesions displacing the chiasm do not show a reduction in visual acuity but rather in the field of view. In fact, for example, Wu et al. (Wu, Duan et al. 2019), using a DTI analysis of a single-shell acquisition and b = 100 s/mm$^2$, found asymmetry in the FA values of the optic nerves of patients with mono-orbital space-occupying lesions who presented reduction in visual acuity and not in reduction of the visual field.

**Anterior optic pathway changes in patients with Leber's Hereditary Optic Neuropathy**

**Introduction**

Leber's hereditary optic neuropathy (LHON) is one of the most common inherited optic neuropathies with an estimated prevalence of about 1:25,000 people (Carelli, Ross-Cisneros et al. 2004, Yu-Wai-Man, Griffiths et al. 2011). In the majority of cases (i.e., > 90%), it is associated with one of three mtDNA missense point mutations (m.3460G>A, m.11778G>A, and m.14484T>C) in genes encoding for the mitochondrial respiratory chain complex I subunits (Maresca, Caporali et al. 2014). LHON is characterized by a sudden, subacute onset of monolateral blindness, commonly followed by blindness in the other eye, and preferentially affects young males. It is characterized by selective loss of RGCs, leading to optic nerve atrophy and varying degrees of blindness in young adulthood.

In normal anatomy, RGC axons are located in the optic head, where they are unmyelinated and therefore have slow conduction velocities. They require a great deal of energy to restore their electrical potentials and have one of the highest oxygen consumptions of all of the tissues in the body. The portions of the optic nerve fibers outside the optic head are made of both axon and a myelin sheath, the latter being composed predominantly of oligodendrocytes and astrocytes. About 5 cm posterior to the optic disk, the two optic nerves converge to form the optic chiasm, where a partial decussation (~53%) occurs (Hansen, Netter et al. 2019).

In histopathological studies of genetically confirmed LHON cases, a complete loss of central fibers with various degrees of axonal sparing in the periphery at the level of the optic head were consistently found (Carelli, Ross-Cisneros et al. 2004). In the myelinated portion of the optic nerve, widely varying myelin thicknesses were also evident, with some axons being almost denuded of myelin sheath. Interestingly, most demyelinated fibers showed accumulations of mitochondria which sometimes completely filled the axonal profile. In some instances, evidence of remyelination was also seen, indicating that the pathophysiological process may be much more dynamic than mere neurodegeneration (Carelli, Ross-Cisneros et al. 2002, Carelli, Ross-Cisneros et al. 2004, Carelli, La Morgia et al. 2017, Maresca and Carelli 2021).

Only two previous studies have attempted to unravel the pathophysiological mechanism responsible for visual deficits in patients with LHON using DTT metrics of the anterior and posterior optic pathways. In 2019, Takemura et al. (Takemura, Ogawa et al. 2019) observed a reduction of FA values both in the anterior optic pathway (in both the chiasm and optic tracts) and in the posterior optic pathway (primarily the optic radiation) in LHON patients compared to normal controls. Interestingly, whereas the reduction of FA only in the chiasma and optic tracts were found to correlate with any other parameter (i.e., reduced T1 value) suggestive of myelin content as a result of the T1 mapping; this was not true for the reduction of FA in the posterior optic pathway. Interestingly, the authors found a reduction in MD in the optic tract only and an increase in MD in the optic radiation.

The authors suggested that the reduction of FA in the two pathways could be related to different biological mechanisms and proposed three possible, although speculative, hypotheses to explain the possibility of different origins of the microstructural changes in the optic radiation. The first is that the reduced FA may reflect axonal dysfunction. Notably, previous ancillary DTI studies in animal models (Aung, Mar et al. 2013) have revealed that diffusivity measurements may be associated with both myelin and axon pathologies. The second, and simplest, hypothesis is that the morphological changes in the myelin of the optic radiation detected as changes in FA do not affect the overall myelin volume fraction parameter calculated by the T1 mapping. The third hypothesis, and potentially the most interesting, is that the alterations in FA may reflect abnormalities in glia in the posterior optic pathway (optic radiation) resulting from reactive gliosis, since this has been observed in an animal model of glaucoma (Bosco, Breen et al. 2016). However, the reductions in FA in the anterior and posterior optic pathways had been observed already previously in 2014 by Ogawa et al. (Ogawa, Takemura et al. 2014) using a tractography paradigm.

The exact pathophysiological mechanism of LHON remains a topic of debate. In a recent OCT follow-up study (Carbonelli, La Morgia et al. 2022), the unaffected eyes of four LHON patients, each with one affected eye, were monitored until they, too, exhibited alterations from 60 days before to 170 days after conversion. The authors found that the primary morphological change was an increase in the thickness of the retinal nerve fiber layer (RNFL), followed by a reduction of the same, whereas the ganglion cell layer (GCL) did not undergo significant changes until the onset of visual loss when a significant reduction of thickness became evident. This poses the question of whether the primary mechanism consists of alterations of the fibers starting from the axons of the RGC (represented in OCT by the RLFN layer) and ultimately reaching the somata of the RGC (represented in OCT by the GCL layers).

The current treatments for LHON are not curative, but recently a gene therapy has been proposed using an intravitreal injection of adeno-associated viral (AAV) vectors, specifically a recombinant replication-defective AAV, serotype 2, which contains a modified complementary DNA encoding the human wild-type mitochondrial NADH dehydrogenase subunit 4 (ND4) protein (Yu-Wai-Man, Newman et al. 2020).

**Aim**

The aim of this current study was to determine whether the DTI metrics evaluated within the tractographic reconstruction of the anterior optic pathways are associated with morphological alteration within the retina and with the progression of the disease after gene therapy.

## Methods

### Study population

All patients with a molecular diagnosis of LHON and no additional atypical findings referred to the Neuroimaging Laboratory by the Laboratory of Neurogenetics at the IRCCS Institute of Neurological Sciences of Bologna, Bellaria Hospital, Bologna, Italy, between April 2021 and January 2022, were considered to be eligible for evaluation. Written informed consent was obtained from patients prior to participation in the study, which was conducted according to the guidelines of the Declaration of Helsinki and approved by the "Area Vasta Emilia Centro" Ethics Committee (CE-AVEC) with approval number NOE-121/2019/OSS/AUSLBO—CE 19012. Patients were included in the subacute phase within nine months from monocular or bilateral onset of visual deficit.

### Study design

Patients received a complete clinical and neuroradiological evaluation the day before intravitreal injection of AAV vector. Gene therapy was administered after approval by the internal ethical committee for compassionate use and signing of the informed consent. We included m.11778/MT-ND4 LHON patients with onset of disease within one year from the last affected eye. Each subject received an intravitreal injection in each eye containing $9 \times 10^{10}$ viral genomes in 90 mL (REFLECT www.clinicaltrials.gov NCT03293524). The procedure was carried out in a surgical room at Bellaria Hospital. Treatment with prophylactic oral steroids was provided. Both clinical and neuroradiological evaluations were repeated at six- and 12-months follow-up for a total of three evaluations.

### Clinical evaluation

Neuro-ophthalmological assessment included the evaluation of the best corrected visual acuity (BCVA) measured using a retro-illuminated Early Treatment Diabetic Retinopathy Study (ETDRS) chart positioned at 4 m and expressed as the logarithm of the minimum angle of resolution (logMAR). Counting fingers and hand movements were converted to 2.0 and 2.3 logMAR, respectively. In this scale blindness is defined as a BCVA worse than 1.3 logMAR (Bailey and Lovie 1976).

OCT for assessing the average RNFL thickness and average GCL thickness (OCT: DRI Triton, Topcon, Tokyo, Japan). OCT images (DRI Triton, Topcon, Tokyo, Japan) were obtained using a 3-dimensional wide scan protocol with a size of 12 × 9 mm consisting of 256 B-scans, each comprising 512 A-scans. Peripapillary RNFL thickness were measured using a 360° 3.4-mm diameter circle scan with thicknesses measured across the superior, nasal, inferior, and temporal sectors and segmentation analysis of the macula measured across six sectors of the 6-mm diameter circular annulus centered on the foveal included GCL. For the purpose of this study, OCT measures were averaged over all assessed retinal areas.

Flash visual evoked potentials (FVEPs) were presented by the ColorDome ganzfeld (Diagnosys LLC). Gold cup skin electrodes were placed in Oz for active, Cz for reference and Fz for. The resulting first and the second positive deflections were named P1 and P2, and their preceding negative deflections, N1 and N2. Peak-to-peak amplitudes (μV) were measured for N1–P1 and N2–P2 complexes. Peak times (ms) were measured for N2 and P2.

The photopic negative response (PhNR) is a slow negative component of a flash photopic full-field electroretinogram (ERG) in which the stimulus conditions were produced also by the ColorDome. Both pupils were dilated (pupil diameter >7 mm) with one drop each of tropicamide 1% and phenylephrine 10% and then light-adapted for 10 min. The corneal surface was anesthetized with two drops of tetracaine 1% to apply Dawson-Trick-Litzkow (DTL-Plus™) micro conductors (Diagnosys LLC, Lowell, MA, USA) on the lower conjunctival fornix. Gold cup electrodes were used in the temple for reference and Fz for ground. Electrode impedance was checked and set at 5 kilo Ohms (kΩ) or less. Red (640 nm) stimulus flashes of 4-ms duration were presented at a 4-Hz rate on a blue (470 nm) rod saturating background. Red flash stimulation was presented at 1, 3 and 7 cd·s/$m^2$, while the blue background remained at 10 kilo Ohms cd/$m^2$. An Espion E3 was used to record PhNR waveforms. A total of six sets of 25 sweeps of 150-ms duration per eye were recorded with bandpass filtering between 0.3 and 300 Hz. Each of the six repetitions was manually filtered to remove eye blink and other motion artifacts, and an average of the remaining responses was generated for each eye. Recordings were obtained from both right and left eyes. PhNR waveforms were visually inspected, and the a-wave, b-wave, and PhNR components were determined. Peak time (ms) and amplitude of PhNR (μV) from peak to trough (amplitude between the peak of the b-wave and the trough of the PhNR) were recorded.

We also retrieved information regarding disease characteristics for all patients included in the study.

**MRI acquisition**

*MRI protocol*

Images were acquired using a 3T MRI Scanner (Magnetom Skyra, Siemens, Erlagen, Germany) and VE11C-SP01 software (maximum gradient amplitude 45 mT $m^{-1}$; maximum "slew rate" 200 T $m^{-1}s^{-1}$) and a 64-channel phased head coil at the IRCSS Istituto delle Scienze Neurologiche di Bologna – Ospedale Bellaria, Bologna.

*Patient preparation*

Written informed consent was obtained from each participant before MRI examination. Participants removed all metallic or non-MRI compatible object before being positioned on the scanner bed in a head-first supine position. Participants were instructed to abstain from rotating their heads inside the coil. Head position was further restricted using foam pads. They used phono-absorbent earplugs to protect their ears from the high noise level. They were also given a bell to ring in case of emergency. The receiver coil has a mirror that allows the patient to see the control room and reduce the effect of claustrophobia.

*Scan protocol*

A standardized scan protocol was followed in which the following sequences were administered. To establish the correct patient placement for setting the reference planes for each sequence, 3-plane localization was implemented from the acquisition console.

T1-weighted images acquired using a three-dimensional inversion recovery prepared spoiled gradient-echo (3D MPRAGE) sequence (flip angle = 9°; TI = 900 ms; TE = 2.98 ms; TR = 2300 ms; acquired matrix size = 256 × 256 × 256; phase FoV = 100%; reconstructed voxel size = 1 mm isotropic) were used as an anatomical reference.

The next sequence was a DTI multi-shell acquisition which employed a single-shot spin-echo EPI sequence with two different phase encoding directions (to better average the useful signal and reduce the effect of eddy currents), A-P and P-A (TE = 98 ms; TR = 4300 ms; 87 contiguous 2-mm thick slices; FoV = 220 × 220 mm; acquired matrix = 110 x 110; reconstructed in-plane resolution = 2.0 mm) with diffusion sensitizing gradients applied in 131 (A-P) and 49 (P-A) non-collinear directions, 8 b = 0 (A-P and P-A), 12 b = 300 s/$mm^2$ (A-P and P-A), 30 b = 1000 s/$mm^2$ (A-P and P-A), 64 b = 2000 s/$mm^2$ (A-P) volumes.

**Diffusion tensor tractography tract estimation**

*Imaging preprocessing*

Data from each participant was preprocessed using an in-house automated pipeline developed from software packages freely available as part of the Oxford FSL, version 6; the NIH AFNI, version

20.3.02; and MRtrix, version 3.0.2. The image format used was compressed NIfTI-1, extension ".nii.gz" (ref: https://nifti.nimh.nih.gov/nifti-1).

DW images were skull-stripped using the FSL "bet" tool. Image denoising was performed with the MRtrix3 "dwidenoise" function (Veraart, Novikov et al. 2016), implementing a principal component analysis approach. Susceptibility-related distortions in the EPI acquisition were estimated using the FSL "topup" function; subsequently, a combined correction for susceptibility, eddy-current effects, and signal dropout, most commonly induced by subject movement, was performed by FSL "eddy_openmp," based on the "topup" estimates.

The DWI data were modelled at the voxel level using functions of the MRtrix toolkit. In particular, the response function for SD was modelled using the "Dhollander" algorithm within "dwi2response" (Dhollander 2019). FODs were estimated using multi-shell multi-tissue SD using the "msmt_csd" method implemented in the "dwi2fod" function (Jeurissen 2014), as described in Manners et al., 2022 (Manners, Gramegna et al. 2022).

Characterization of the diffusion properties of tissue within each voxel was provided by FSL "dtifit" based on the diffusion tensor, which was used to estimate voxel FA and MD.

*Tract estimation*

The MRtrix tool "tckgen" generated these streamlines by an iFOD1 approach (Tournier, J.-D.; Calamante, F 2012), following the procedure described by He et al. (He, Zhang et al. 2021).

In order to isolate the anterior optic pathway, selected fibers were transformed to the NIfTI format to create a volumetric probability map based on fiber density. Voxels were subjected to a threshold that excluded low probability tracts as detailed in the following section.

**Anterior optic pathway reconstruction**

*Processing*

On the MNI152 standard brain, a mask was drawn that included the trajectory of the whole anterior optic pathway from the optic bulb to the LGN (called "NERVO_mask"). A single automatic exclusion ROI was then created, including all the possible spurious segment originating from the principal tract (called "ROI_NERVO_excl"). Next, a seed from the LGN ("ROI_II_LGN"), an inclusion ROI in the optic chiasm ("ROI_II_chiasm"), and a target ("ROI_II_orbit") were defined.

An affine registration was performed between the $b_0$ image of the DWI and the 3D MPRAGE T1 using the "flirt" tool in FSL while a non-linear deformation of the 3D MPRAGE T1 to the MNI standard space was performed using "fnirt" of FSL, in order to indirectly transformation between the $b_0$ image to MNI space. This registration is applied to each ROI with the "applywarp" function (using the "nearest neighbour" approach for the mask and the exclusion and the "trilinear approach" for the others). For each hemisphere (Left=L and Right=R), the iFOD1 ("tckgen") method was applied to generate up to 5 million streamlines from the LGN ROI (seed), then

selecting only those fulfilling specified criteria: angle ≤ 10°, cutoff/seed_cutoff = 0.005, crossing the ROI of the chiasma and reaching the ipsilateral or contralateral ROI of the orbit (target). The seeding eventually stopped if 1000 streamlines were selected according to the above constraints. As a result, the four possible combinations of crossing (LR, RL) or non-crossing (LL, RR) tracks were separately reconstructed. The same procedure was repeated after inverting the seed and the target and the pairs of corresponding tracks by seed and target were added into a single tract. The tracts were then transformed into an image in the NIfTI format, where the voxel intensity was proportional to the density of the streamlines; finally, a threshold set at 10% of the maximum value was applied to obtain the final tract mask.

*Along-tract analysis*

In order to perform the along-tract analysis, the "final_nifti" file is used to mask each of the streamline file defining the two tracks (right orbit tract- left geniculate and left orbit tract- right geniculate). For each of these tracks, the streamline file is registered to the MNI using the "tcktransform" option. For each tract, the most extreme points are defined as the most extreme points that are reached by at least 50% of the fibers in the anterior and posterior directions. To identify them, the nerve is cut in each slice of the NIfTI image in the main direction of the nerve (typically the y-axis) and the number of streamlines passing through each slice is calculated using the "tckedit + tckstats" option of MRtrix. (Tournier, Smith, Ret al. 2019) .The two identified extreme points of each track define a line, which is used to do the resampling (using the "tckresample" function) of each line in 15 equidistant points. Segments 1-7 are those corresponding to the optic tract, segments 7-9 to the optic chiasm, and segments 10-15 to the optic nerves.

**DTI metrics definition**

For each of the 15 segments the DTI-derived metrics MD and FA are calculated and averaged for the right optic nerve fibers reaching the left geniculate ganglion and the left optic nerve reaching the right geniculate ganglion.

**Statistical analysis**

Descriptive and frequency statistics were calculated using Excel, and comparisons were computed using IBM SPSS Statistics 22.0.

Pearson's correlation (r) was used to evaluate the relationship between clinical and ophthalmological variables (time since visual deficit onset, logMAR, average RNFL, average PhNP amplitude, average PhNP latency, average GCL) over each patient and each assessment time point. The relationship between mean MD and FA values were assessed against each of the six clinical variables in two ways.

Firstly, simple regression was used to regress the MR variable against each clinical variable, including each eye separately, but only the first time point (before treatment). Then, a mixed model regression was performed, adding the patient as a random variable, to evaluating changes between assessment time points.

Correlation parameters (r) and regression models (F) were considered to be significant when the calculated probability was < 5%. Jamovi v. 2.3 was used for statistical analyses. The module GAMlj 2.6.6 was used for mixed model regression.

**Results**

*Study population*

At baseline, nine patients were included (mean age ± standard deviation = 24.9 ± 15.7 years, range 14-54). Six out of nine patients (mean age 35.0 ± 12.3 years, range 19-54) were included in follow-up study (two examinations).

*Clinical and OCT evaluation at baseline and follow-up*

At baseline examination, the mean time from disease onset was 9.1 ± 4.6 months (range = 4 - 19.5 months). At OCT evaluation, the mean logMAR results were 65.3 ± 23.6 (range = 1.3 - 2.3. The mean RNFL thickness was 65.3 ± 23.6 μm (range = 35.0 – 108). The mean GCl thickness was 40.5 ± 5.3 μm (range = 32.7 - 50.5). The mean PhNR amplitude was -19.28 ± 8.88 μV (range = 36.72 – 7.88). The mean PhNR latency was 66.7 ± 3.0 μV (range = 61 –73).

At the first follow-up, the mean time from disease onset was 16.9 ± 4.8 months (range = 10 - 25.5 months). At OCT evaluation, the mean logMAR results were 1.5 ± 0.4 (range = 1.1 – 2.0). The mean RNFL average thickenss was 60.4 ± 8.4 μm (range = 51.0 - 76.0). The mean GCl average thickness was 41.7±4.9 μm (range = 34.7 – 50.3). The mean PhNR average amplitude was -14.18 ± 6.68μV (range = -28.1 – -3.1). The mean PhNR average latency was 70.4 ± 5.0 μV (range = 62.0 – 77.0).

At the second follow-up, the mean time from disease onset was 23.8 ± 4.7 months (range = 16 - 29.5). At OCT evaluation, the mean logMAR results were 1.3 ± 0.3 (range = 0.8 – 1.6). The mean RNFL average thickness was 50.6 ± 11.2 μm (range = 40 - 76. The mean GCl average thickness was 40.4 ± 4.5 μm (range = 33.7 – 48.7). The mean PhNR average amplitude was -11.83 ± 5.78 μV (range = -26.4 – -42). The mean PhNR average latency was 71.6 ± 3.4 μV (range = 65.0 – 78.5).

**DTI metrics**

At baseline examination, the mean FA value in the anterior optic pathway was 0.259 ± 0.0319 (range = 0.22 - 0.30. At first follow-up the mean FA value of the anterior optic pathway was 0.2591 ± 0.027 (range = 0.22 - 0.33). At second follow-up the mean FA value of the anterior optic pathway was 0.2392 ± 0.0289 (range = 0.21 - 0.29). There was a trend towards a reduction in the mean FA values (p = 0.065)

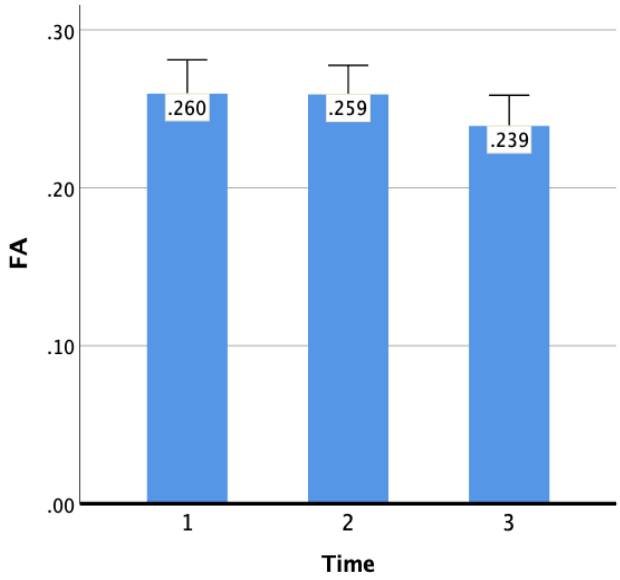


At baseline examination, the mean MD was 1.283 ± 0.2218 (range = 0.86 – 1.64). At first follow-up, the mean MD was 1.358 ± 0.155 (range = 1.18 - 1.63). At second follow-up the mean MD was 1.52 ± 0.198 (range = 1.24 - 1.82). There was a statistically significant increase in MD over time (p = 0.002).

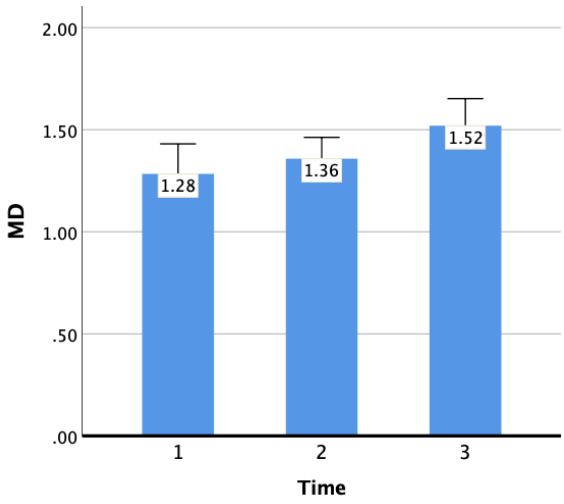

**Correlations between Clinical, OCT and DTI metrics**

Time from onset correlated with both logMAR (r = -0.525, p = < 0.001) and RNLF (r = -0.603, p = < 0.001). The RNLF correlated with the PhNR amplitude values (r = -0.457, p = 0.004) and PhNR latency values (r = -0.471, p = 0.002). PhNR amplitude values were correlated with the GCL (r = -0.468, p = 0.003).

Considering the mean MD at baseline, a regression analysis showed a significantly correlation with the time from onset (p < .001), the RNFL mean value averages (p < .001), and PhNR amplitude (p < .001) and PhNR latency (p = 0.015).

Considering the mean MD changes over time, a regression analysis showed only a significant association with RNFL average reduction (p = 0.036).

Considering the mean FA at baseline, a regression analysis showed a significantly correlation with time from onset (p=0.009), RNFL average reduction (p < .001) and PhNR average amplitude (p = 0.003).

No clinical parameters were associated with FA changes over time.

Referring to Figure4, RNFL correlated negatively with time since onset, and the two PhNP indicators, which correlated with each other. Visual acuity (logMAR) also correlated with time since onset. GCL only correlated with PhNP amplitude.

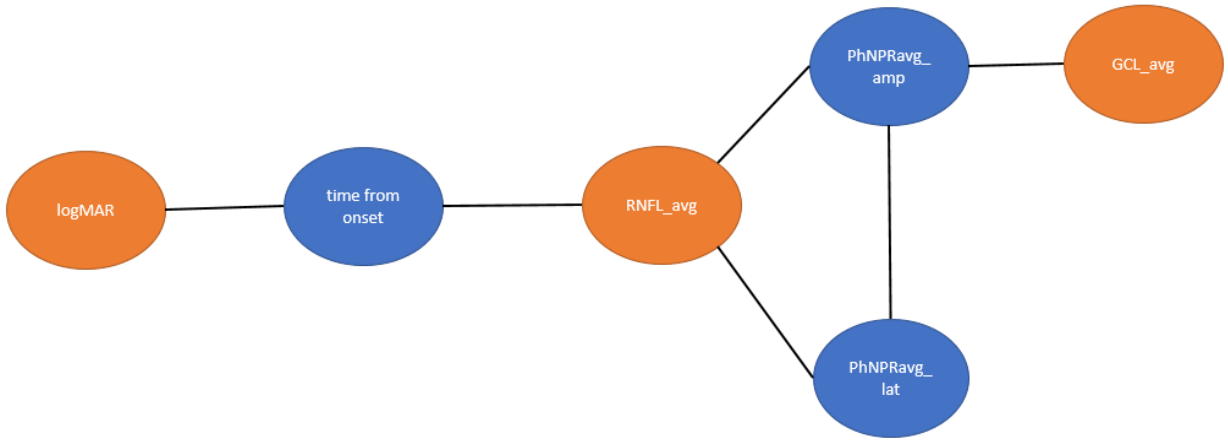


**Figure 6**. Clinical and ophthalmological variables found to correlate significantly. Variables of the same color are positively correlated, while those of different colors are negatively correlated.
Considering only the first time point, mean MD was significantly correlated to RNFL (p = 0.036), while FA showed a trend towards the same relationship (p = 0.054). Considering the changes between different time points, MD continued to show a significant dependency on RFNL, but also on time since onset, and the two PhNP parameters. FA was dependent on RNFL, time since onset, and PhNP amplitude.

Considering all of the results, RNFL was the clinical/ophthalmological variable showing the most consistent relationship to the MR diffusion variables.

**Discussion**

In this part of the thesis, I have explored the association of anterior optic tract DTI metrics with clinical, OCT, and electrophysiological markers of disease severity in LHON. We also correlated the progression of the DTI metrics with the clinical progression of the disease over a 12-month follow-up and response to an innovative genetic therapy.

*At the baseline examination,* this study demonstrates that both MD and FA median values within the anterior optic pathway (considering the total myelinated nerve course from the retrobulbar region of the optic nerve until the contralateral LGN) are directly correlated with retinal RNFL reduction, with worse retinal electrophysiological response function amplitude, and with time from onset of the disease. This is an important finding as it demonstrated that the pathological alterations evaluated in the retina are reflected in the MD and FA values within the anterior optic pathway.

*After baseline*, our patients were evaluated at six and 12 months after bilateral intravitreal injection of recombinant replication-defective AAV (rAAV2/2-ND4). This was possible after the positive finding of the REVERSE phase 3 clinical trial that had previously evaluated the efficacy of a single intravitreal injection of rAAV2/2-ND4 in subjects with visual loss from LHON (Yu-Wai-Man, Newman et al. 2020), after the preliminary positive result of efficiently rescue an induced defect in mitochondrial respiratory chain complex I in a rat model of the disease (Cwerman-Thibault, Augustin et al. 2015). However, it is interesting to keep in mind that in the REVERSE trial there was an unexpected improvement in visual function in the contralateral untreated eye after unilateral intravitreal administration of the viral vector. In an attempt to shed light on the possible mechanism for this phenomenon, the authors subsequently performed a nonhuman primate study, injecting viral DNA in a monolateral eye of a monkey and found, in a post-mortem study, evidence of transfer of viral vector DNA from the injected eye to the contralateral retina, optic nerve, and chiasm at three months follow-up (Yu-Wai-Man, Newman et al. 2020). The authors interpret this finding as a possible trans-synaptic or trans-neuronal transfer mechanism (Zingg, Chou et al. 2017) or contamination between mitochondria present in the WM tract originating from the right retina directed towards the left geniculate and those originating from the left retina and directed towards the right geniculate nucleus when they intersect within the chiasma (Mandal and Drerup 2019). Mitochondria have been shown to migrate long distances in axons to distribute energy and allow for distal neuronal activity (A. Mandal, 2019). Mitochondria may also be exported through astrocytes that are found at a high density in the optic nerve head (Burdett and Freeman 2014). Finally, the dense network of interconnected astrocytes could have aided this process via membrane junctions (Ariazi, Benowitz et al. 2017).

In our follow-up study, only the progressive increase in MD in the anterior optic tract was significantly associated with the progressive decrease in RNFL layers thickness, as was expected by the natural history of the disease. Our results, therefore, suggest that the isotropic component of diffusion, as demonstrated by the pathological increase in MD, may best reflect the pathological

changes in the nerve fiber at the level of the optic nerve, chiasm, and tracts after viral injection, which are associated to the reduction in RNFL.

It is established that the interpretations of altered DTI metrics are not univocal and may depend on different biological mechanisms according to the disease studied (*Dhollander T* 2021). In a recent *post-mortem* and DTI study in which the author provoked a unilateral retinal ischemia in ten rats, which were subsequently sacrificed and subjected to a 7-Tesla examination with a high-resolution DTI sequence using a 3-dimensional echo-planar acquisition (TR/TE= 250/21 ms; voxel size = 125 x 125 x 125 $\mu m^3$, 80 different gradient directions, b-values of 2000 and 2500 $s/mm^2$, total scanning time = 15 h) (Narvaez-Delgado, Rojas-Vite et al. 2019). The post-mortem histological results of both the intact and pathologic nerves are interesting. In the intact optic nerve, they observed tightly packed axons with dense, circular myelin sheaths as well as interstitial glial cells and their processes, some of them encircling capillaries. On the contrary, in the injured optic nerves they observed an abnormal microstructure, involving both axons and surrounding glial elements (in which the glial process appeared to increase in size and number associated with foamy phagocytes) with shrunken axoplasm and retracted myelin sheaths. However, the total thickness of myelin sheaths tended to be larger in the injured nerves, likely due to the pathological separation of individual myelin layers and intra-myelin inclusions, as depicted by electron microscopic observation. The number of axons was considerably lower as compared to intact nerves, reducing axonal density by around 50%, which translated into reductions in axon and myelin volume fractions. The remaining structurally viable axons in the injured nerves tended to have slightly larger calibers, with a proportionally larger loss of small-caliber axons (Narvaez-Delgado, Rojas-Vite et al. 2019).

The authors analyzed different non-common methods of modeling the DTI data acquired at 7 T. Among their metrics, the only one comparable with one of those acquired in our paradigm is the FA results of a multi-resolution discrete search (MRDS) algorithm of analysis. They unexpectedly found that the FA of the optic nerves and chiasm negatively correlates with myelin thickness and axon diameter (meaning that higher FA was present in the case of smaller myelin thickness and axonal diameter). A subsequent examination using electron microscopy revealed that myelin thickness was overestimated by the method used for automatic segmentation because of the abundance of intra-myelin inclusions and fraying of myelin sheaths in pathological cases. These findings provide a basis to suggest that microstructural pathological change in the myelin in pathological optic nerve and tract after therapy may not be reflected in changes in FA.

The absence of correlation with the clinical data of increased visual acuity (i.e., logMAR) suggest that the increase in visual acuity may be independent from the progression of microstructural alterations within the pathway, thus suggesting a possible central mechanism of cortical plasticity, perhaps at the level of the geniculate ganglion.

Overall, this part of my thesis demonstrates that both MD and FA metrics in the anterior optic pathway may be alternative objective biomarkers that directly reflect intracranial anterior optic

pathway pathophysiology in patients with LHON. These biomarkers should be used in the evaluation of new therapeutic strategies.

**Conclusions**

In my Ph.D. thesis, I have demonstrated a cutting-edge implementation of DTI acquisition, using a combination of HARDI (i.e., more than 30 gradient diffusion direction) and MULTISHELL sequences (i.e., multiple non-zero b values), on a clinically available 3-Tesla scanner with an acquisition time (i.e., 12 min) that is compatible with clinical protocols. Moreover, in collaboration with the Technical Development Group (TDG) of the Neuroimaging Laboratory we have developed the first algorithm, based on a combination of tools from open-source software made available by the international scientific community (FSL, MRtrix, AFNI) able to automatically reconstruct the whole course of CN II (including the whole anterior optic pathway) as well the olfactory nerve.

This important practical achievement has allowed us to implement the automatic tractographic reconstruction of the whole displaced anterior optic pathway in patients with sellar/parasellar tumors, providing important information for presurgical planning. Apart from being the largest case series published on this topic, this has allowed us to find an interesting reduction in MD in the displaced chiasma of these patients. Our results suggest that the anisotropic component of diffusion (in the tensor model made by DTI), may be a better indicator of pathological changes reflecting displacement and/or compression of extracranial myelinated nerve. This finding provides a basis for possible use in future studies of anisotropic diffusion metrics in cases of displacement and compression of peripheral nerves.

The same acquisition technology has allowed us to study a genetic disease involving the anterior optic pathway, namely LHON, in which the successful reconstruction of the entire anterior optic pathway was able to depict the association between the microstructural parameters within the whole pathway and electrophysiological marker of dysfunction of the optic nerve as well as the reduction in axonal nerve fiber layer in the retina itself. Moreover, we were able to follow the responses of patients to the therapy. This study provides a basis for the introduction of whole non-invasive optic pathway MRI biomarkers both for disease activity and follow-up assessment.

Regarding the reconstruction of CN I, the absence of a significant difference between COVID-19 patients and healthy controls demonstrates the necessity of developing new signal modeling strategies able to improve the reconstruction of fibers in this area in presence of inevitable partial volume contamination in voxels containing air in the sinus cavities.

**References**


Akazawa, K., K. Yamada, S. Matsushima, M. Goto, S. Yuen and T. Nishimura (2010). "Optimum b value for resolving crossing fibers: a study with standard clinical b value using 1.5-T MR." Neuroradiology **52**(8): 723-728.

Alexander, A. L. (2010). Deterministic White Matter Tractography. Diffusion MRI: Theory, Methods, and Applications. P. D. K. Jones, Oxford University Press**.**

Anderson, A. W. (2001). "Theoretical analysis of the effects of noise on diffusion tensor imaging." Magn Reson Med **46**(6): 1174-1188.

Anik, I., Y. Anik, K. Koc, S. Ceylan, H. Genc, O. Altintas, D. Ozdamar and D. Baykal Ceylan (2011). "Evaluation of early visual recovery in pituitary macroadenomas after endoscopic endonasal transphenoidal surgery: Quantitative assessment with diffusion tensor imaging (DTI)." Acta Neurochirurgica **153**(4): 831-842.

Ariazi, J., A. Benowitz, V. De Biasi, M. L. Den Boer, S. Cherqui, H. Cui, N. Douillet, E. A. Eugenin, D. Favre, S. Goodman, K. Gousset, D. Hanein, D. I. Israel, S. Kimura, R. B. Kirkpatrick, N. Kuhn, C. Jeong, E. Lou, R. Mailliard, S. Maio, G. Okafo, M. Osswald, J. Pasquier, R. Polak, G. Pradel, B. de Rooij, P. Schaeffer, V. A. Skeberdis, I. F. Smith, A. Tanveer, N. Volkmann, Z. Wu and C. Zurzolo (2017). "Tunneling Nanotubes and Gap Junctions-Their Role in Long-Range Intercellular Communication during Development, Health, and Disease Conditions." Front Mol Neurosci **10**: 333.

Assaf, Y. and P. J. Basser (2005). "Composite hindered and restricted model of diffusion (CHARMED) MR imaging of the human brain." Neuroimage **27**(1): 48-58.

Aung, W. Y., S. Mar and T. L. Benzinger (2013). "Diffusion tensor MRI as a biomarker in axonal and myelin damage." Imaging Med **5**(5): 427-440.

Bailey, I. L. and J. E. Lovie (1976). "New design principles for visual acuity letter charts." Am J Optom Physiol Opt **53**(11): 740-745.

Barletta-Rodolfi, C., F. Gasparini and E. Ghidoni (2011). "Kit del neuropsicologo italiano." Bologna: Società Italiana di Neuropsicologia.

Basser, P. J., J. Mattiello and D. LeBihan (1994). "Estimation of the effective self-diffusion tensor from the NMR spin echo." J Magn Reson B **103**(3): 247-254.

Baumann, P. S., L. Cammoun, P. Conus, K. Q. Do, P. Marquet, D. Meskaldji, R. Meuli, J. P. Thiran and P. Hagmann (2012). "High b-value diffusion-weighted imaging: a sensitive method to reveal white matter differences in schizophrenia." Psychiatry Res **201**(2): 144-151.

Beaulieu, C. (2002). "The basis of anisotropic water diffusion in the nervous system - a technical review." NMR Biomed **15**(7-8): 435-455.

Behrens, T. E., H. J. Berg, S. Jbabdi, M. F. Rushworth and M. W. Woolrich (2007). "Probabilistic diffusion tractography with multiple fibre orientations: What can we gain?" Neuroimage **34**(1): 144-155.

Bosco, A., K. T. Breen, S. R. Anderson, M. R. Steele, D. J. Calkins and M. L. Vetter (2016). "Glial coverage in the optic nerve expands in proportion to optic axon loss in chronic mouse glaucoma." Exp Eye Res **150**: 34-43.

Brooks, D. E., A. M. Komàromy and M. E. Källberg (1999). "Comparative retinal ganglion cell and optic nerve morphology." Vet Ophthalmol **2**(1): 3-11.

Burdett, T. C. and M. R. Freeman (2014). "Neuroscience. Astrocytes eyeball axonal mitochondria." Science **345**(6195): 385-386.

Buschhüter, D., M. Smitka, S. Puschmann, J. C. Gerber, M. Witt, N. D. Abolmaali and T. Hummel (2008). "Correlation between olfactory bulb volume and olfactory function." Neuroimage **42**(2): 498-502.

Caffarra, P., G. Vezzadini, F. Dieci, F. Zonato and A. Venneri (2002). "Rey-Osterrieth complex figure: normative values in an Italian population sample." Neurological Sciences **22**(6): 443-447.

Capoulade, J., M. Wachsmuth, L. Hufnagel and M. Knop (2011). "Quantitative fluorescence imaging of protein diffusion and interaction in living cells." Nature Biotechnology **29**(9): 835-839.

Carbonelli, M., C. La Morgia, M. Romagnoli, G. Amore, P. D'Agati, M. L. Valentino, L. Caporali, M. L. Cascavilla, M. Battista, E. Borrelli, A. Di Renzo, V. Parisi, N. Balducci, V. Carelli and P. Barboni (2022). "Capturing the Pattern of Transition From Carrier to Affected in Leber Hereditary Optic Neuropathy." Am J Ophthalmol **241**: 71-79.

Carelli, V., C. La Morgia, F. N. Ross-Cisneros and A. A. Sadun (2017). "Optic neuropathies: the tip of the neurodegeneration iceberg." Human Molecular Genetics **26**(R2): R139-R150.

Carelli, V., F. N. Ross-Cisneros and A. A. Sadun (2002). "Optic nerve degeneration and mitochondrial dysfunction: genetic and acquired optic neuropathies." Neurochem Int **40**(6): 573-584.

Carelli, V., F. N. Ross-Cisneros and A. A. Sadun (2004). "Mitochondrial dysfunction as a cause of optic neuropathies." Prog Retin Eye Res **23**(1): 53-89.

Carlesimo, G. A., C. Caltagirone and G. Gainotti (1996). "The Mental Deterioration Battery: normative data, diagnostic reliability and qualitative analyses of cognitive impairment. The Group for the Standardization of the Mental Deterioration Battery." Eur Neurol **36**(6): 378-384.

Castellaro, M., M. Moretto, V. Baro, S. Brigadoi, E. Zanoletti, M. Anglani, L. Denaro, R. Dell'Acqua, A. Landi, F. Causin, D. d'Avella and A. Bertoldo (2020). "Multishell Diffusion MRI-Based Tractography of the Facial Nerve in Vestibular Schwannoma." AJNR Am J Neuroradiol **41**(8): 1480-1486.

Clark, C. A. and D. Le Bihan (2000). "Water diffusion compartmentation and anisotropy at high b values in the human brain." Magn Reson Med **44**(6): 852-859.

Clifford-Jones, R. E., W. I. McDonald and D. N. Landon (1985). "Chronic optic nerve compression. An experimental study." Brain **108 ( Pt 1)**: 241-262.

Collantes, M. E. V., A. I. Espiritu, M. C. C. Sy, V. M. M. Anlacan and R. D. G. Jamora (2021). "Neurological Manifestations in COVID-19 Infection: A Systematic Review and Meta-Analysis." Can J Neurol Sci **48**(1): 66-76.

Cwerman-Thibault, H., S. Augustin, C. Lechauve, J. Ayache, S. Ellouze, J. A. Sahel and M. Corral-Debrinski (2015). "Nuclear expression of mitochondrial ND4 leads to the protein assembling in complex I and prevents optic atrophy and visual loss." Mol Ther Methods Clin Dev **2**: 15003.

Dasenbrock, H. H., S. A. Smith, A. Ozturk, S. K. Farrell, P. A. Calabresi and D. S. Reich (2011). "Diffusion tensor imaging of the optic tracts in multiple sclerosis: association with retinal thinning and visual disability." J Neuroimaging **21**(2): e41-49.

Dhollander, T., R. Mito, D. Raffelt and A. Connelly (2019). "Improved white matter response function estimation for 3-tissue constrained spherical deconvolution." Proc Intl Soc Mag Reson Med **555**.

Douaud, G., S. Lee, F. Alfaro-Almagro, C. Arthofer, C. Wang, P. McCarthy, F. Lange, J. L. R. Andersson, L. Griffanti, E. Duff, S. Jbabdi, B. Taschler, P. Keating, A. M. Winkler, R. Collins, P. M. Matthews, N. Allen, K. L. Miller, T. E. Nichols and S. M. Smith (2022). "SARS-CoV-2 is associated with changes in brain structure in UK Biobank." Nature **604**(7907): 697-707.

Drake, R., A. W. Vogl and A. W. M. Mitchell (2020). Gray's Anatomy for Students - Elsevier eBook on VitalSource.

Duprez, T. P. and P. Rombaux (2010). "Imaging the olfactory tract (cranial nerve #1)." Eur J Radiol **74**(2): 288-298.

Echevarria-Cooper, S. L., G. Zhou, C. Zelano, F. Pestilli, T. B. Parrish and T. Kahnt (2022). "Mapping the Microstructure and Striae of the Human Olfactory Tract with Diffusion MRI." The Journal of Neuroscience **42**(1): 58-68.

Eida, S., M. Van Cauteren, Y. Hotokezaka, I. Katayama, M. Sasaki, M. Obara, T. Okuaki, M. Sumi and T. Nakamura (2016). "Length of intact plasma membrane determines the diffusion properties of cellular water." Scientific Reports **6**(1): 19051.

Einstein, A. (1905). "Über die von der molekularkinetischen Theorie der Wärme geforderte Bewegung von in ruhenden Flüssigkeiten suspendierten Teilchen." Annalen der Physik **322**(8): 549-560.

Gala, F. (2015). "Magnetic resonance imaging of optic nerve." Indian J Radiol Imaging **25**(4): 421-438.
García Santos, J. M., C. Ordóñez and S. Torres del Río (2008). "ADC measurements at low and high b values: insight into normal brain structure with clinical DWI." Magn Reson Imaging **26**(1): 35-44.

Ge, M., S. Li, L. Wang, C. Li and J. Zhang (2015). "The role of diffusion tensor tractography in the surgical treatment of pediatric optic chiasmatic gliomas." J Neurooncol **122**(2): 357-366.

Hajiabadi, M., M. Alimohamadi and R. Fahlbusch (2015). "Decision Making for Patients With Concomitant Pituitary Macroadenoma and Ophthalmologic Comorbidity: A Clinical Controversy." World Neurosurgery **84**(1): 147-153.

Hajiabadi, M., M. Samii and R. Fahlbusch (2016). "A preliminary study of the clinical application of optic pathway diffusion tensor tractography in suprasellar tumor surgery: preoperative, intraoperative, and postoperative assessment." J Neurosurg **125**(3): 759-765.

Hales, P. W., V. Smith, D. Dhanoa-Hayre, P. O'Hare, K. Mankad, F. d'Arco, J. Cooper, R. Kaur, K. Phipps, R. Bowman, D. Hargrave and C. Clark (2018). "Delineation of the visual pathway in paediatric optic pathway glioma patients using probabilistic tractography, and correlations with visual acuity." Neuroimage Clin **17**: 541-548.

Hansen, J. T., F. H. Netter and C. A. G. Machado (2019). Netter's Clinical Anatomy. Philadelphia, PA, Elsevier.

He, J., F. Zhang, G. Xie, S. Yao, Y. Feng, D. C. A. Bastos, Y. Rathi, N. Makris, R. Kikinis, A. J. Golby and L. J. O'Donnell (2021). "Comparison of multiple tractography methods for reconstruction of the retinogeniculate visual pathway using diffusion MRI." Hum Brain Mapp **42**(12): 3887-3904.

Helwany, M. and B. Bordoni (2022). Neuroanatomy, Cranial Nerve 1 (Olfactory). StatPearls. Treasure Island (FL), StatPearls PublishingCopyright © 2022, StatPearls Publishing LLC.

Hofer, S., A. Karaus and J. Frahm (2010). "Reconstruction and dissection of the entire human visual pathway using diffusion tensor MRI." Front Neuroanat **4**: 15.

J. Salazar, J., A. I. Ramírez, R. De Hoz, E. Salobrar-Garcia, P. Rojas, J. A. Fernández-Albarral, I. López-Cuenca, B. Rojas, A. Triviño and J. M. Ramírez (2019). Anatomy of the Human Optic Nerve: Structure and Function, IntechOpen.

Jacquesson, T., F. Cotton, A. Attyé, S. Zaouche, S. Tringali, J. Bosc, P. Robinson, E. Jouanneau and C. Frindel (2019). "Probabilistic Tractography to Predict the Position of Cranial Nerves Displaced by Skull Base Tumors: Value for Surgical Strategy Through a Case Series of 62 Patients." Neurosurgery **85**(1): E125-e136.

Jeurissen, B., J. D. Tournier, T. Dhollander, A. Connelly and J. Sijbers (2014). "Multi-tissue constrained spherical deconvolution for improved analysis of multi-shell diffusion MRI data." Neuroimage **103**: 411-426.
Jin, Z., Y. Bao, Y. Wang, Z. Li, X. Zheng, S. Long and Y. Wang (2019). "Differences between generalized Q-sampling imaging and diffusion tensor imaging in visualization of crossing neural fibers in the brain." Surg Radiol Anat **41**(9): 1019-1028.

Jones, D. K. (2008). "Tractography gone wild: probabilistic fibre tracking using the wild bootstrap with diffusion tensor MRI." IEEE Trans Med Imaging **27**(9): 1268-1274.

Jones, D. K., T. R. Knösche and R. Turner (2013). "White matter integrity, fiber count, and other fallacies: the do's and don'ts of diffusion MRI." Neuroimage **73**: 239-254.

Jones, D. K. and C. Pierpaoli (2005). "Confidence mapping in diffusion tensor magnetic resonance imaging tractography using a bootstrap approach." Magn Reson Med **53**(5): 1143-1149.

Kamali, A., K. M. Hasan, P. Adapa, A. Razmandi, Z. Keser, J. Lincoln and L. A. Kramer (2014). "Distinguishing and quantification of the human visual pathways using high-spatial-resolution diffusion tensor tractography." Magn Reson Imaging **32**(7): 796-803.

Kammen, A., M. Law, B. S. Tjan, A. W. Toga and Y. Shi (2016). "Automated retinofugal visual pathway reconstruction with multi-shell HARDI and FOD-based analysis." Neuroimage **125**: 767-779.

Kobal, G., T. Hummel, B. Sekinger, S. Barz, S. Roscher and S. Wolf (1996). ""Sniffin' sticks": screening of olfactory performance." Rhinology **34**(4): 222-226.

Koch, M. A., D. G. Norris and M. Hund-Georgiadis (2002). "An investigation of functional and anatomical connectivity using magnetic resonance imaging." Neuroimage **16**(1): 241-250.

Larson, R. D. (2013). "Psychometric Properties of the Modified Fatigue Impact Scale." International Journal of MS Care **15**(1): 15-20.

Lazar, M. and A. L. Alexander (2003). "An error analysis of white matter tractography methods: synthetic diffusion tensor field simulations." Neuroimage **20**(2): 1140-1153.
Le Bihan, D. (2007). "The 'wet mind': water and functional neuroimaging." Phys Med Biol **52**(7): R57-90.

Le Bihan, D. (2013). "Apparent diffusion coefficient and beyond: what diffusion MR imaging can tell us about tissue structure." Radiology **268**(2): 318-322.

Le Bihan, D. and H. Johansen-Berg (2012). "Diffusion MRI at 25: exploring brain tissue structure and function." Neuroimage **61**(2): 324-341.

Liang, L., H. Lin, F. Lin, J. Yang, H. Zhang, L. Zeng, Y. Hu, W. Lan, H. Zhong, H. Zhang, S. Luo, Y. Mo, W. Li and Y. Lei (2021). "Quantitative visual pathway abnormalities predict visual field defects in patients with pituitary adenomas: a diffusion spectrum imaging study." Eur Radiol **31**(11): 8187-8196.

Lober, R. M., R. Guzman, S. H. Cheshier, D. R. Fredrick, M. S. B. Edwards and K. W. Yeom (2012). "Application of diffusion tensor tractography in pediatric optic pathway glioma: Clinical article." Journal of Neurosurgery: Pediatrics PED **10**(4): 273-280.
López-Elizalde, R., A. Campero, T. Sánchez-Delgadillo, Y. Lemus-Rodríguez, M. López-González and M. Godínez-Rubí (2018). "Anatomy of the olfactory nerve: A comprehensive review with cadaveric dissection." Clinical Anatomy **31**(1): 109-117.

Lovibond, P. F. and S. H. Lovibond (1995). "The structure of negative emotional states: Comparison of the Depression Anxiety Stress Scales (DASS) with the Beck Depression and Anxiety Inventories." Behaviour research and therapy **33**(3): 335-343.

Ma, J., S. Su, S. Yue, Y. Zhao, Y. Li, X. Chen and H. Ma (2016). "Preoperative Visualization of Cranial Nerves in Skull Base Tumor Surgery Using Diffusion Tensor Imaging Technology." Turk Neurosurg **26**(6): 805-812.

Maingard, J. and R. Sharma. (2022). "Frontal lobe."

Maleki, N., L. Becerra, J. Upadhyay, R. Burstein and D. Borsook (2012). "Direct optic nerve pulvinar connections defined by diffusion MR tractography in humans: implications for photophobia." Hum Brain Mapp **33**(1): 75-88.

Mandal, A. and C. M. Drerup (2019). "Axonal Transport and Mitochondrial Function in Neurons." Front Cell Neurosci **13**: 373.

Manners, D. N., L. L. Gramegna, C. La Morgia, G. Sighinolfi, C. Fiscone, M. Carbonelli, M. Romagnoli, V. Carelli, C. Tonon and R. Lodi (2022). "Multishell Diffusion MR Tractography Yields Morphological and Microstructural Information of the Anterior Optic Pathway: A Proof-of-Concept Study in Patients with Leber's Hereditary Optic Neuropathy." Int J Environ Res Public Health **19**(11).

Maresca, A., L. Caporali, D. Strobbe, C. Zanna, D. Malavolta, C. La Morgia, M. L. Valentino and V. Carelli (2014). "Genetic Basis of Mitochondrial Optic Neuropathies." Curr Mol Med **14**(8): 985-992.

Maresca, A. and V. Carelli (2021). "Molecular Mechanisms behind Inherited Neurodegeneration of the Optic Nerve." Biomolecules **11**(4): 496.

Martin, J. H. (2021). The gustatory, visceral afferent, and olfactory systems. Neuroanatomy: Text and Atlas, 5e. J. H. Martin. New York, NY, McGraw Hill**:** 223-246.

Mehraeen, E., F. Behnezhad, M. A. Salehi, T. Noori, H. Harandi and S. SeyedAlinaghi (2021). "Olfactory and gustatory dysfunctions due to the coronavirus disease (COVID-19): a review of current evidence." Eur Arch Otorhinolaryngol **278**(2): 307-312.

Mikami, T., Y. Minamida, T. Yamaki, I. Koyanagi, T. Nonaka and K. Houkin (2005). "Cranial nerve assessment in posterior fossa tumors with fast imaging employing steady-state acquisition (FIESTA)." Neurosurg Rev **28**(4): 261-266.

Milner, B. (1971). "Interhemispheric differences in the localization of psychological processes in man." Br Med Bull **27**(3): 272-277.

Minckler, D. S. (1980). "The organization of nerve fiber bundles in the primate optic nerve head." Arch Ophthalmol **98**(9): 1630-1636.
Mito, R., T. Dhollander, Y. Xia, D. Raffelt, O. Salvado, L. Churilov, C. C. Rowe, A. Brodtmann, V. L. Villemagne and A. Connelly (2020). "In vivo microstructural heterogeneity of white matter lesions in healthy elderly and Alzheimer's disease participants using tissue compositional analysis of diffusion MRI data." Neuroimage Clin **28**: 102479.

Mohammadi, S., M. Gouravani, M. A. Salehi, H. Harandi, F. Moosaie, F. Dehghani Firouzabadi and D. M. Yousem (2022). "Olfactory system measurements in COVID-19: a systematic review and meta-analysis." Neuroradiology: 1-15
.
Mori, S., B. J. Crain, V. P. Chacko and P. C. van Zijl (1999). "Three-dimensional tracking of axonal projections in the brain by magnetic resonance imaging." Ann Neurol **45**(2): 265-269.

Mori, S. and P. C. van Zijl (2002). "Fiber tracking: principles and strategies - a technical review." NMR Biomed **15**(7-8): 468-480.

Naidich, T. P., M. Castillo, S. Cha and J. G. Smirniotopoulos (2012). Imaging of the Brain: Expert Radiology Series, Elsevier Health Sciences.

Naismith, R. T., J. Xu, N. T. Tutlam, S. Lancia, K. Trinkaus, S. K. Song and A. H. Cross (2012). "Diffusion tensor imaging in acute optic neuropathies: predictor of clinical outcomes." Arch Neurol **69**(1): 65-71.

Narvaez-Delgado, O., G. Rojas-Vite, R. Coronado-Leija, A. Ramírez-Manzanares, J. L. Marroquín, R. Noguez-Imm, M. L. Aranda, B. Scherrer, J. Larriva-Sahd and L. Concha (2019). "Histological and diffusion-weighted magnetic resonance imaging data from normal and degenerated optic nerve and chiasm of the rat." Data Brief **26**: 104399.

Nasreddine, Z. S., N. A. Phillips, V. Bédirian, S. Charbonneau, V. Whitehead, I. Collin, J. L. Cummings and H. Chertkow (2005). "The Montreal Cognitive Assessment, MoCA: a brief screening tool for mild cognitive impairment." J Am Geriatr Soc **53**(4): 695-699.
"NIfTI-1 Data Format." from https://nifti.nimh.nih.gov/nifti-1.

Novelli, G., C. Papagno, E. Capitani, N. L'aiacona, G. Vallar and S. F. Cappa (1986). "Tre test clinici di ricerca e produzione lessicale, Taratura su soggetti normali." Archivo di psicologia neurologia e psichiatria **47**: 477-506.

Nucifora, P. G., R. Verma, S. K. Lee and E. R. Melhem (2007). "Diffusion-tensor MR imaging and tractography: exploring brain microstructure and connectivity." Radiology **245**(2): 367-384.

O'Donnell, L. J. and C. F. Westin (2011). "An introduction to diffusion tensor image analysis." Neurosurg Clin N Am **22**(2): 185-196, viii.

Ogawa, S., H. Takemura, H. Horiguchi, M. Terao, T. Haji, F. Pestilli, J. D. Yeatman, H. Tsuneoka, B. A. Wandell and Y. Masuda (2014). "White matter consequences of retinal receptor and ganglion cell damage." Invest Ophthalmol Vis Sci **55**(10): 6976-6986.

Oldfield, R. C. (1971). "The assessment and analysis of handedness: The Edinburgh inventory." Neuropsychologia **9**(1): 97-113.
Oleszkiewicz, A., V. A. Schriever, I. Croy, A. Hähner and T. Hummel (2019). "Updated Sniffin' Sticks normative data based on an extended sample of 9139 subjects." European Archives of Oto-Rhino-Laryngology **276**(3): 719-728.

Orsini, A. and C. Laicardi (1998). WAIS-R Contributo alla Taratura Italiana, Giunti Organizzazioni Speciali.

Parker, G. J., H. A. Haroon and C. A. Wheeler-Kingshott (2003). "A framework for a streamline-based probabilistic index of connectivity (PICo) using a structural interpretation of MRI diffusion measurements." J Magn Reson Imaging **18**(2): 242-254.

Parker, G. J. M. (2010). Probabilistic Fiber Tracking. Diffusion MRI: Theory, Methods, and Applications. P. D. K. Jones, Oxford University Press**:** 0.

Paul, D. A., E. Gaffin-Cahn, E. B. Hintz, G. J. Adeclat, T. Zhu, Z. R. Williams, G. E. Vates and B. Z. Mahon (2014). "White matter changes linked to visual recovery after nerve decompression." Science translational medicine **6**(266): 266ra173.

Pierpaoli, C., P. Jezzard, P. J. Basser, A. Barnett and G. Di Chiro (1996). "Diffusion tensor MR imaging of the human brain." Radiology **201**(3): 637-648.

Pines, A. R., M. Cieslak, B. Larsen, G. L. Baum, P. A. Cook, A. Adebimpe, D. G. Dávila, M. A. Elliott, R. Jirsaraie, K. Murtha, D. J. Oathes, K. Piiwaa, A. F. G. Rosen, S. Rush, R. T. Shinohara, D. S. Bassett, D. R. Roalf and T. D. Satterthwaite (2020). "Leveraging multi-shell diffusion for studies of brain development in youth and young adulthood." Dev Cogn Neurosci **43**: 100788.

Puzniak, R. J., K. Ahmadi, J. Kaufmann, A. Gouws, A. B. Morland, F. Pestilli and M. B. Hoffmann (2019). "Quantifying nerve decussation abnormalities in the optic chiasm." Neuroimage Clin **24**: 102055.

Raz, N., A. S. Bick, A. Klistorner, S. Spektor, D. S. Reich, T. Ben-Hur and N. Levin (2015). "Physiological Correlates and Predictors of Functional Recovery After Chiasmal Decompression." Journal of Neuro-Ophthalmology **35**(4).

Reitan, R. M. and D. Wolfson (2001). The Halstead–Reitan Neuropsychological Test Battery: Research findings and clinical application. Specific learning disabilities and difficulties in children and adolescents: Psychological assessment and evaluation. New York, NY, US, Cambridge University Press**:** 309-346.

Rey, A. (1964). L'examen clinique en psychologie. Paris, Presses universitaires de France.

Roebroeck, A., R. Galuske, E. Formisano, O. Chiry, H. Bratzke, I. Ronen, D. S. Kim and R. Goebel (2008). "High-resolution diffusion tensor imaging and tractography of the human optic chiasm at 9.4 T." Neuroimage **39**(1): 157-168.

Seo, H. S., K. H. Chang, D. G. Na, B. J. Kwon and D. H. Lee (2008). "High b-value diffusion (b = 3000 s/mm2) MR imaging in cerebral gliomas at 3T: visual and quantitative comparisons with b = 1000 s/mm2." AJNR Am J Neuroradiol **29**(3): 458-463.

Sisto, D., M. Trojano, M. Vetrugno, T. Trabucco, G. Iliceto and C. Sborgia (2005). "Subclinical visual involvement in multiple sclerosis: a study by MRI, VEPs, frequency-

doubling perimetry, standard perimetry, and contrast sensitivity." Invest Ophthalmol Vis Sci **46**(4): 1264-1268.

Skorpil, M., T. Rolheiser, H. Robertson, A. Sundin and P. Svenningsson (2011). "Diffusion tensor fiber tractography of the olfactory tract." Magn Reson Imaging **29**(2): 289-292.

Stejskal, E. O. and J. E. Tanner (1965). "Spin Diffusion Measurements: Spin Echoes in the Presence of a Time-Dependent Field Gradient." The Journal of Chemical Physics **42**(1): 288-292.

Tadakuma, H., Y. Ishihama, T. Shibuya, T. Tani and T. Funatsu (2006). "Imaging of single mRNA molecules moving within a living cell nucleus." Biochem Biophys Res Commun **344**(3): 772-779.

Takemura, H., S. Ogawa, A. A. Mezer, H. Horiguchi, A. Miyazaki, K. Matsumoto, K. Shikishima, T. Nakano and Y. Masuda (2019). "Diffusivity and quantitative T1 profile of human visual white matter tracts after retinal ganglion cell damage." NeuroImage: Clinical **23**: 101826.

Techavipoo, U., A. F. Okai, J. Lackey, J. Shi, M. A. Dresner, T. P. Leist and S. Lai (2009). "Toward a practical protocol for human optic nerve DTI with EPI geometric distortion correction." J Magn Reson Imaging **30**(4): 699-707.

Tournier, J.-D., F. Calamante and A. Connelly (2012). "MRtrix: Diffusion tractography in crossing fiber regions." International Journal of Imaging Systems and Technology **22**(1): 53-66.

Tournier, J. D., F. Calamante and A. Connelly (2007). "Robust determination of the fibre orientation distribution in diffusion MRI: non-negativity constrained super-resolved spherical deconvolution." Neuroimage **35**(4): 1459-1472.

Tournier, J. D., F. Calamante and A. Connelly (2013). "Determination of the appropriate b value and number of gradient directions for high-angular-resolution diffusion-weighted imaging." NMR Biomed **26**(12): 1775-1786.

Tournier, J. D., F. Calamante, D. G. Gadian and A. Connelly (2004). "Direct estimation of the fiber orientation density function from diffusion-weighted MRI data using spherical deconvolution." Neuroimage **23**(3): 1176-1185.

Tournier, J. D., R. Smith, D. Raffelt, R. Tabbara, T. Dhollander, M. Pietsch, D. Christiaens, B. Jeurissen, C. H. Yeh and A. Connelly (2019). "MRtrix3: A fast, flexible and open software framework for medical image processing and visualisation." Neuroimage **202**: 116137.

Veraart, J., D. S. Novikov, D. Christiaens, B. Ades-Aron, J. Sijbers and E. Fieremans (2016). "Denoising of diffusion MRI using random matrix theory." Neuroimage **142**: 394-406.

Wärntges, S. and G. Michelson (2014). "Detailed illustration of the visual field representation along the visual pathway to the primary visual cortex: a graphical summary." Ophthalmic Res **51**(1): 37-41.

Wu, C. N., S. F. Duan, X. T. Mu, Y. Wang, P. Y. Lan, X. L. Wang and K. C. Li (2019). "Assessment of optic nerve and optic tract alterations in patients with orbital space-occupying lesions using probabilistic diffusion tractography." Int J Ophthalmol **12**(8): 1304-1310.

Yoshino, M., K. Abhinav, F. C. Yeh, S. Panesar, D. Fernandes, S. Pathak, P. A. Gardner and J. C. Fernandez-Miranda (2016). "Visualization of Cranial Nerves Using High-Definition Fiber Tractography." Neurosurgery **79**(1): 146-165.

Yu-Wai-Man, P., P. G. Griffiths and P. F. Chinnery (2011). "Mitochondrial optic neuropathies - disease mechanisms and therapeutic strategies." Prog Retin Eye Res **30**(2): 81-114.

Yu-Wai-Man, P., N. J. Newman, V. Carelli, M. L. Moster, V. Biousse, A. A. Sadun, T. Klopstock, C. Vignal-Clermont, R. C. Sergott, G. Rudolph, C. La Morgia, R. Karanjia, M. Taiel, L. Blouin, P. Burguière, G. Smits, C. Chevalier, H. Masonson, Y. Salermo, B. Katz, S. Picaud, D. J. Calkins and J. A. Sahel (2020). "Bilateral visual improvement with unilateral gene therapy injection for Leber hereditary optic neuropathy." Sci Transl Med **12**(573).

Zingg, B., X. L. Chou, Z. G. Zhang, L. Mesik, F. Liang, H. W. Tao and L. I. Zhang (2017). "AAV-Mediated Anterograde Transsynaptic Tagging: Mapping Corticocollicular Input-Defined Neural Pathways for Defense Behaviors." Neuron **93**(1): 33-47.

Zolal, A., S. B. Sobottka, D. Podlesek, J. Linn, B. Rieger, T. A. Juratli, G. Schackert and H. H. Kitzler (2017). "Comparison of probabilistic and deterministic fiber tracking of cranial nerves." J Neurosurg **127**(3): 613-621.

**MR in vivo tractography for the reconstruction of cranial nerves course**

ABSTRACT

**Aim**

The aim of my Ph.D. was to implement a diffusion tensor tractography (DTT) pipeline to reconstruct cranial nerve I (olfactory) to study COVID-19 patients, and anterior optic pathway (AOP, including optic nerve, chiasm, and optic tract) to study patients with sellar/parasellar tumors, and with Leber's Hereditary Optic Neuropathy (LHON).

**Methods**

We recruited 23 patients with olfactory dysfunction after COVID-19 infection (mean age 37±14 years, 12 females); 27 patients with sellar/parasellar tumors displacing the optic chiasm eligible for endonasal endoscopic surgery (mean age 53. ±16.4 years, 13 female) and 6 LHON patients (mutation 11778/MT-ND4, mean age 24.9±15.7 years). Sex- and age-matched healthy control were also recruited.

In LHON patients, optical coherence tomography (OCT) was performed. Acquisitions were performed on a clinical high field 3-T MRI scanner, using a multi-shell HARDI (High Angular Resolution Diffusion Imaging) sequence (b-values 0-300-1000-2000 s/mm$^2$, 64 maximum gradient directions, 2mm$^3$ isotropic voxel). DTT was performed with a multi-tissue spherical deconvolution approach and mean diffusivity (MD) DTT metrics were compared with healthy controls using an unpaired t-test. Correlations of DTT metrics with clinical data were sought by regression analysis.

**Results**

In all 23 hypo/anosmic patients with previous COVID-19 infection the CN I was successfully reconstructed with no DTT metrics alterations, thus suggesting the pathogenetic role of central olfactory cortical system dysfunction.

In all 27 patients with sellar/parasellar tumors the AOP was reconstructed, and in 11/13 (84.7%) undergoing endonasal endoscopic surgery the anatomical fidelity of the reconstruction was confirmed; a significant decrease in MD within the chiasma ($p<0.0001$) was also found.

In LHON patients a reduction of MD in the AOP was significantly associated with OCT parameters ($p=0.036$).

**Conclusions**

Multi-shell HARDI diffusion-weighted MRI followed by multi-tissue spherical deconvolution for the DTT reconstruction of the CN I and AOP has been implemented, and its utility demonstrated in clinical practice.